Photonic Time-Stretched Analog-to-Digital Converter: Fundamental Concepts and Practical Considerations

Yan Han and Bahram Jalali, *Fellow, IEEE*

Invited Paper

***Abstract*—Ultra-wide-band analog-to-digital (A/D) conversion is one of the most critical problems faced in communication, instrumentation, and radar systems. This paper presents a comprehensive analysis of the recently proposed time-stretched A/D converter. By reducing the signal bandwidth prior to digitization, this technique offers revolutionary enhancements in the performance of electronic converters. The paper starts with a fundamental-physics analysis of the time–wavelength transformation and the implication of time dilation on the signal-to-noise ratio. A detailed mathematical description of the time-stretch process is then constructed. It elucidates the influence of linear and nonlinear optical dispersion on the fidelity of the electrical signal. Design issues of a single-sideband time-stretch system, as they relate to broad-band operation, are examined. Problems arising from the nonuniform optical power spectral density are explained, and two methods for overcoming them are described. As proof of the concept, 120 GSa/s real-time digitization of a 20-GHz signal is demonstrated. Finally, design issues and performance features of a continuous-time time-stretch system are discussed.**

***Index Terms*—Analog-to-digital (A/D) conversion, microwave photonics, optical signal processing, single-sideband (SSB) modulation, time stretch.**

I. Introduction

DIGITAL signal processing (DSP) has revolutionized modern communication and radar systems by offering unprecedented performance and adaptivity. For broad-band systems, however, the application of DSP is hindered by difficulty in capturing the wide-band signal [1]. A sampling oscilloscope is not an option because it requires the signal to be repetitive in time. It only provides information about the average signal behavior; hence, it does not operate in real time. The real-time capture of ultrafast electrical signals is a difficult problem that requires wide-band analog-to-digital converters (ADCs).

Manuscript received April 15, 2003; revised July 29, 2003. This work was supported by the Defense Advanced Research Project Agency (DARPA) under the Photonic Analog-to-Digital Converter (PACT) program.

The authors are with Optoelectronic Circuits and Systems Laboratory, Department of Electrical Engineering, University of California at Los Angeles, Los Angeles, CA 90095 USA (e-mail: jalali@ucla.edu).

Digital Object Identifier 10.1109/JLT.2003.821731

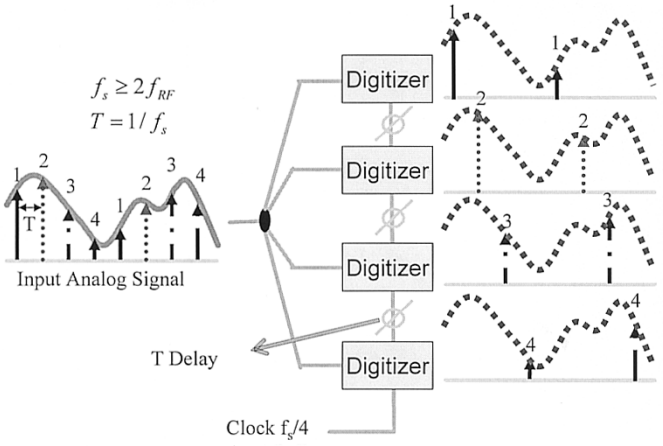

Fig. 1. Conventional sample-interleaved ADC architecture. The signal is captured by a parallel array of slow digitizer, each clocked at a fraction of the Nyquist rate. The Nyquist criterion is only satisfied when the signal is reconstructed, sample-by-sample, in the digital domain.

A detailed discussion on the limits of electronic ADCs is beyond the scope of this paper [2]. Simply stated, the performance is limited by one or more of the following problems:

1) jitter in the sampling clock;
2) settling time of the sample-and-hold circuit;
3) speed of the comparator (comparator ambiguity);
4) mismatches in the transistor thresholds and passive component values.

The limitations imposed by all these factors become more severe at higher frequencies.

The standard approach to deal with this problem is to employ parallelism through the use of the time-interleaved ADC architecture, shown in Fig. 1 [3], [4]. Here, the signal is captured by a parallel array of slow digitizers, each clocked at a fraction of the Nyquist rate. The Nyquist criterion is only satisfied when the signal is reconstructed, sample-by-sample, in the digital domain. In this paper, we use the term "*sample-interleaved*" to refer to this architecture. It is well known that mismatches between digitizers limit the dynamic range and, hence, the resolution of sample-interleaved ADC systems [3], [4]. A state-of-the-art electronic ADC, embodied by real-time digitizing oscilloscopes (Tektronix TDS7404, or Agilent 54 854A) boasts 20 GSa/s 4-GHz analog bandwidth. Depending on the

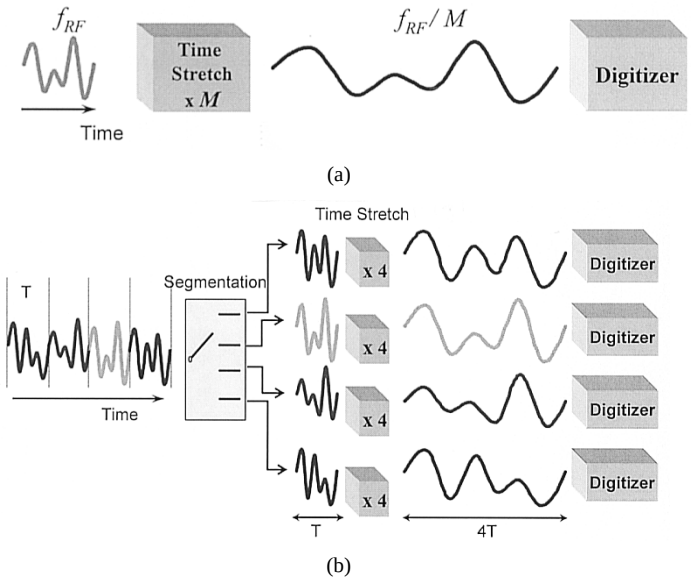

Fig. 2. Conceptual block diagram for the time-stretched ADC. (a) Single-channel system for capturing a time-limited signal. (b) Multichannel system for capturing a continuous-time signal. In contrast to the sample-interleaved system (Fig. 1), each channel here is sampled at or above the Nyquist rate.

input signal amplitude, these instruments exhibit an effective number-of-bits (ENOB) of approximately 4–5.5 b, measured over the full bandwidth.

An entirely new A/D architecture is the so-called *time-stretched* ADC, shown in Fig. 2[5]–[7]. Here, the analog signal is slowed down prior to sampling and quantization by an electronic digitizer. For a time-limited input, a single channel, shown in Fig. 2(a), suffices. A continuous-time input can be captured with a multichannel system, as shown in Fig. 2(b). The partitioning of the continuous signal into parallel segments does not necessarily require electronic switches. As discussed subsequently in this paper, it can be performed passively in the optical domain.

Slowing down the signal prior to digitization has several advantages. For a stretch factor of M, the effective sampling rate of the electronic digitizer f_s is increased to $M \cdot f_s$. The effective input bandwidth of the electronic digitizer is also increased by M. The error associated with the jitter in the sampling clock of the digitizer is reduced due to a reduction in the signal slew rate, a key feature not shared by the conventional sample-interleaved architecture. For a time-limited input, only a single digitizer is needed [Fig. 2(a)]. Hence, interchannel mismatch problems are avoided as there is no need to use multiple digitizers. For the continuous-time system [Fig. 2(b)], one would expect the similar interchannel mismatches; however, it has recently been shown that mismatch errors can be corrected using the information available in the signal [8]. This is another advantage of the *time-stretched* ADC (TS-ADC) over the *sample-interleaved* ADC. It exploits a fundamental difference between the two systems: in the former, the signal at each channel is sampled at or above the Nyquist rate, whereas in the latter, it is sampled at a fraction of the Nyquist rate.

A practical method for implementing the time-stretch function is to use the photonic technique shown in Fig. 3 [7], [9]. A linearly chirped optical pulse is generated by propagating the broad-band (nearly transform-limited) pulses generated by a SC source [10] in a chromatic dispersive medium, such as the single-mode fiber (SMF). The electrical input signal modulates the intensity of the chirped optical pulses in an electrooptic modulator (EOM). The envelope is subsequently stretched in a second spool of fiber before photodetection and digitization by a moderate-speed electronic ADC.

This paper discusses fundamental and practical considerations of time-stretched ADC. Section II explains the validity of the linear time–wavelength mapping, a central assumption in the time-stretch technique. The influence of time stretching on an electrical signal-to-noise ratio (SNR) is discussed in the next section. Section IV describes a detailed analytical model for the time-stretch process that reveals the effects of linear and nonlinear fiber dispersion on the fidelity of the time-stretched signal. Section V provides an explanation of the time–bandwidth product (TBP), and its dependence on physical system parameters. It identifies the limit on the TBP set by dispersion and identifies single-sideband (SSB) modulation as a means to mitigate it. In Section VI, practical limitation of SSB modulation is discussed, and it is shown that an ultra-wide-band system can be constructed using commercially available components. Section VII describes the differential time-stretch technique and its ability to remove distortion caused by spectral nonuniformity and pulse-to-pulse variations of the optical source. Finally, Section VIII discusses the fundamental and practical considerations for continuous-time operation of the time-stretch ADC.

II. Time–Wavelength Mapping

An intuitive approach to understanding the time-stretch process is through the time–wavelength mapping representation. The stretch process consists of two steps. Step 1 is the time-to-wavelength (t-to-λ) mapping performed by the combination of the chirped optical pulse and the EOM. As shown in the subset of Fig. 3, 1-ps pulses generated by a passively mode-locked fiber laser at 1560 nm are used to generate broad-band supercontinuum (SC) in three stages of fibers after the amplification [10]. An optical bandpass filter is placed after SC generation to slice a suitable portion for time stretching. The so-obtained nearly transform-limited optical pulse is chirped after propagating through a dispersive medium. When this chirped pulse is modulated by an intensity modulator, the time-domain signal is mapped into wavelength domain. Step 2 is the wavelength-to-time (λ-to-t) mapping performed by the second fiber. The modulated chirped pulse propagates through a second dispersive medium. As a result, the signal modulated onto the chirp pulse is stretched in the time as the pulse is further chirped.

The validity of time–wavelength representation can be understood through the following argument. Suppose that the chirped pulse is obtained by linearly dispersing a transform-limited pulse of the width Δt_o. This represents the system's time resolution; in other words, time cannot be localized beyond Δt_o. Hence, the wavelength-to-time mapping picture is only valid when the time scale of interest is sufficiently larger than this time ambiguity. The time scale of interest depends on

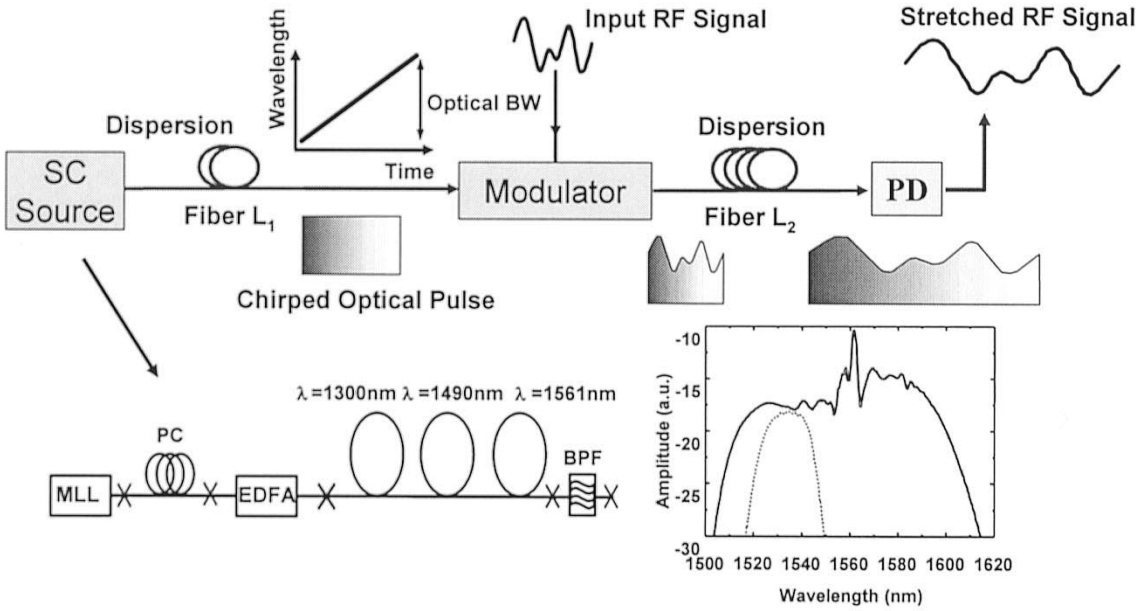

Fig. 3. Functional block diagram for the photonic time-stretch preprocessor. A linearly chirped optical pulse is obtained by dispersing an ultra-short ultra-wide-band pulse (the SC). Time-to-wavelength mapping is achieved when this pulse is intensity-modulated by the electrical signal. The inset is the diagram of a three-stage SC generation. SC: Supercontinuum. PD: Photodetector.

the speed of the electrical signal. The well-known Nyquist sampling theorem states that it is enough to sample a band-limited signal with the maximum frequency $\omega_{\rm RF}$ at the sample interval of $\Delta T = \pi/\omega_{\rm RF}$, without the loss of information. To map the time scale of an electrical signal with frequency $\omega_{\rm RF}$ to optical wavelength, it is required that $\Delta t_o \ll \pi/\omega_{\rm RF}$. Fundamentally, Δt_o is related to the optical bandwidth $\omega_{\rm opt}$ by the uncertainty principle $\omega_{\rm opt}\Delta t_o \geq 1/2$. Relating optical and electrical bandwidths, the combination of uncertainty and Nyquist principles imply that the time–wavelength mapping representation is valid as long as $\omega_{\rm RF} \ll 2\pi\omega_{\rm opt}$. Typically, $\omega_{\rm opt}$ is in the terahertz range, whereas $\omega_{\rm RF}$ is in the gigahertz range. Therefore, the assumption is readily justified.

The time-stretch system, as described previously, relies on the linear group-velocity dispersion (GVD) characterized by the GVD parameter β_2 to linearly stretch the radio-frequency (RF) waveform in time. However, it is well known that the optical fiber possesses nonlinear GVD, i.e., GVD is a function of wavelength. The wavelength dependence of GVD is characterized by the higher order terms in the expansion of β as a function of frequency, namely, β_3, β_4, etc. Wavelength-dependent GVD may distort the RF signal since different time segments may be stretched by different amounts. In other words, the stretch factor can be time dependent. In this section, we analyze this phenomenon and demonstrate that the nonlinear dispersion has no effect on the stretch factor in the time-stretch system. This fortuitous effect occurs because the effect in the two fibers counteract.

The GVD in optical fibers is conveniently described in terms of the dispersion parameter $D(\lambda)$. As an example, we consider $D(\lambda)$ for the SMF-28 fiber, which in units of picoseconds/kilometers/nanometers is given by (according to the Corning SMF-28 product information sheet)

$$D(\lambda) = \frac{S_0}{4}\left(\lambda - \frac{\lambda_0^4}{\lambda^3}\right) \tag{1}$$

where λ_0 is the zero-dispersion wavelength and S_0 is dispersion slope at λ_0. After traveling through a unit length of fiber, the time–wavelength transformation is governed by the GVD. The group delay per unit length is described by

$$\tau_g(\lambda) = \int_{\lambda_{\rm REF}}^{\lambda} D(\lambda)d\lambda = \frac{S_0}{8}\left(\lambda^2 + \frac{\lambda_0^4}{\lambda^2} - \lambda_{\rm REF}^2 - \frac{\lambda_0^4}{\lambda_{\rm REF}^2}\right)$$

where $\lambda_{\rm REF}$ represents the reference wavelength. Then, at the input to the modulator, the input time scale is related to the wavelength as

$$t_{\rm in} = L_1 \cdot \tau_{g1}(\lambda) \tag{2}$$

where L_1 is the length of the first fiber and τ_{g1} is the τ_g for the fiber 1. At the output of fiber 2, the output time scale and wavelength are related by

$$t_{\rm out} = L_1 \cdot \tau_{g1}(\lambda) + L_2 \cdot \tau_{g2}(\lambda) \tag{3}$$

where L_2 is the second fiber length and τ_{g2} is the τ_g for the fiber 2. It can be clearly seen that as long as the two fibers have identical dispersion characteristics ($\tau_{g1} = \tau_{g2}$), the time transformation from the input to output is linear and can be simply described by

$$t_{\rm out} = \frac{(L_1 + L_2)}{L_1} \times t_{\rm in} = M \cdot t_{\rm in} \tag{4}$$

where we define the magnification factor (or the stretch factor) $M = (L_1 + L_2)/L_1$. The wavelength dependence of GVD (described by β_3 and higher order terms) are cancelled and, hence, do not cause a nonuniform stretch.

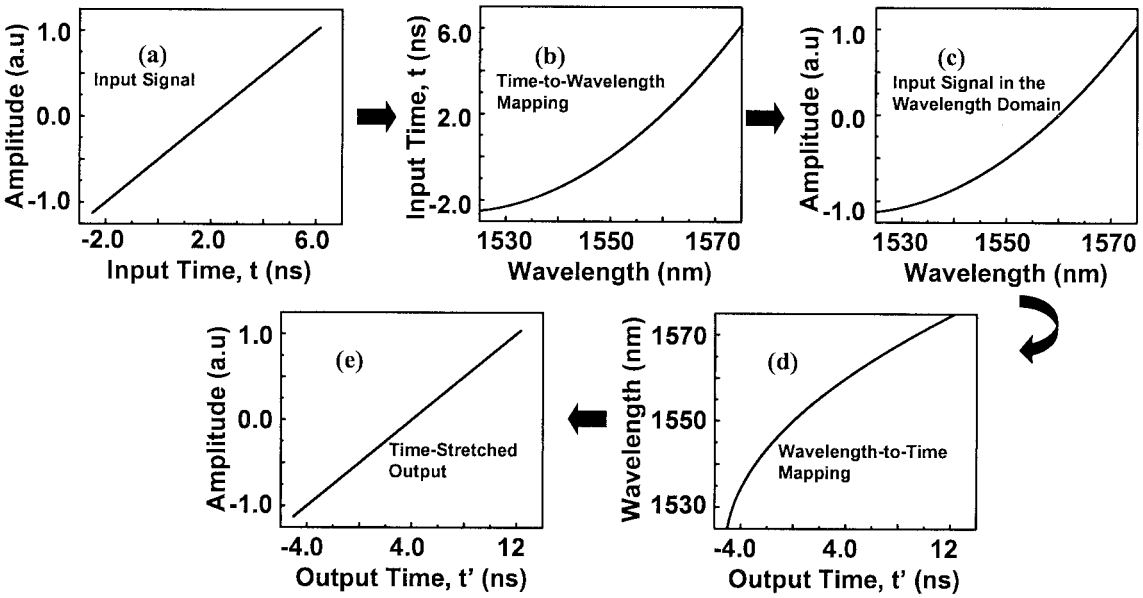

Fig. 4. Graphical description of the time–wavelength transformation. (a) Input signal. (b) Time–wavelength transfer function associated with nonlinear dispersion in fiber 1. (c) Input signal after time-to-wavelength mapping. (d) Wavelength–time transfer function after fiber 2. (e) Output time-stretched signal. The stretch process is linear (uniform) despite the nonlinear fiber dispersion.

A physical understanding can be obtained from Fig. 4, which shows the evolution of the signal through the system. To highlight the effect of wavelength-dependent GVD, we use a value $\beta_3 = 1$ ps^3/km which is an order of magnitude higher than that in the SMF (SMF 28). For simplicity, we consider a linear ramp for the input signal, shown in Fig. 4(a). It corresponds to the RF signal at the modulator input in Fig. 3. Assuming operation in the anomalous dispersion regime of the fiber, the t-to-λ mapping is not linear and, in particular, has positive concavity, as shown in Fig. 4(b). This results in an apparent distortion of the signal when the time-domain signal is mapped into the wavelength domain by modulating the ramp signal on the chirped pulse, as shown in Fig. 4(c). However, the λ-to-t mapping in the second fiber has the opposite curvature, as shown in Fig. 4(d), resulting in a linear (and stretched) output after the photodetection, shown in Fig. 4(e). As shown previously, this property is independent of length of fibers (hence, independent of the stretch factor) as long as the two fibers have identical dispersion behaviors. As will be shown by a more detailed model in Section IV, β_3 does cause another form of distortion through its interaction with the optical modulator. In addition, small differences in the dispersion property (GVD per unit length) of the two fibers will result in a finite amount of wavelength-dependent (and, hence, time-dependent) stretch factor.

We now summarize the key parameters of the TS-ADC: the stretch factor, time aperture, and electrical bandwidth. Through (1)–(4), it was shown that the stretch factor is given by $M = 1 + L_2/L_1$, or more generally, $M = 1 + D_{t,2}/D_{t,1}$, where $D_{t,1}$ and $D_{t,2}$ represent the total dispersion in each dispersive element. The time aperture in a single-channel system, or the segment length in the case of continuous-time operation (see Fig. 2), is equal to the chirped pulse duration at the modulator input. This is given by $T_A = \Delta\lambda D_1 L_1$, where D_1 is the dispersion parameter of fiber 1, and $\Delta\lambda$ is the optical bandwidth. Here, it is assumed that the chirped pulsewidth is much larger than initial nearly transform-limited pulsewidth. As an example, assuming 20-nm optical bandwidth and 500-ps/nm dispersion (roughly equivalent to a spool of dispersion-compensating fiber (DCF) with a 3-dB total loss), the time aperture T_A is 10 ns. Another important system parameter is the 3-dB electrical bandwidth. As will be shown in Section IV, in the case of double-sideband intensity modulation, dispersion limits the 3-dB bandwidth to $\Delta f_{\mathrm{RF}} = [1/(8\pi\,|\beta_2|\,L_2/M)]^{1/2}$.

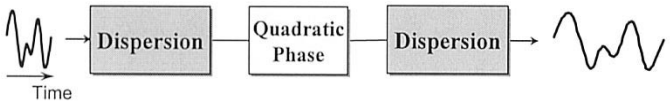

Fig. 5. Conceptual diagram of time-lens system exploiting the analogy between paraxial diffraction and temporal dispersion. In contrast, in the time-stretch system, the input signal is not dispersed prior to receiving the linear chirp (or quadratic phase) due to the lack of low-loss wide-band electrical dispersive devices. The time-stretch system with the application of magnifying an electrical signal is different than the time lens with the application of magnifying an optical signal.

Finally, we point out the difference between the time-stretch system described here and the time-lens concept [5], [11]. Shown in Fig. 5, the latter exploits the analogy between paraxial diffraction and temporal dispersion to magnify an optical waveform. The input signal is first dispersed, then linearly chirped (quadratic phase shifted) and finally dispersed again. For applications to A/D conversion, the input signal is electrical. The lack of low-loss wide-band electrical dispersive devices renders the time lens inapplicable to A/D conversion. In the time-stretch system, a linear chirp is imposed onto the signal by the combination of the chirped optical pulse and the EOM. The input signal is not dispersed prior to receiving the linear chirp. Hence, the system is not a time lens. The main consequence of this deviation from an ideal time lens is the limitation on bandwidth of signal that can be stretched. This topic is discussed in Section IV.

III. Impact of Time-Stretch on SNR

Intuitively, one would expect a reduction in the signal power upon time stretching. This would be rather undesirable if it impacts the SNR. In this section, we analyze this phenomenon and show that, serendipitously, there is no impact on the shot- and thermal-noise-limited SNR. In addition, we show that time stretching alleviates the SNR reduction due to the jitter in the sampling clock. We also explain the impact of optical amplifiers when used to mitigate losses in the time-stretch system.

The shot-noise-limited SNR in a given electrical bandwidth B_e can be written as

$$\mathrm{SNR}_{\mathrm{shot}} = \frac{\langle i \rangle}{2eB_e} \tag{5}$$

where $\langle i \rangle$ is the average photocurrent, and e is the electron charge. For a lossless system, when the signal is stretched by the factor of M, the average signal power and, hence, $\langle i \rangle$ are reduced by M in order to preserve the total energy. At the same time, since the signal is slowed down, the required receiver bandwidth is reduced by M. In other words, both the numerator and the denominator in (5) are reduced by the same amount factor, rendering the $\mathrm{SNR}_{\mathrm{shot}}$ unchanged.

With respect to thermal noise, the corresponding SNR is given by

$$\mathrm{SNR}_{\mathrm{thermal}} = \frac{\langle i \rangle^2 R_{\mathrm{equ}}}{4kTB_e} \propto \frac{\langle i \rangle^2}{4kTB_e^2 C} \tag{6}$$

where k is the Boltzman constant, T is the temperature, R_{equ} and C are the equivalent input resistance and the total input capacitance of the optical-to-electrical (O/E) receiver. After time stretching, both $\langle i \rangle$ and B_e are reduced by M; hence, the thermal-noise-limited SNR also remains unchanged.

When the analog signal is sampled prior to quantization, an additional noise is produced by the jitter in the sampling clock. This so-called aperture uncertainty error is the main obstacle to achieving a high resolution in a high-speed A/D converter [2]. The resulting SNR is related to the root-mean-square (rms) jitter τ_j as

$$\mathrm{SNR}_{\mathrm{jitter}} = \frac{1}{8\pi^2 f_{\mathrm{RF}}^2 \tau_j^2} \tag{7}$$

where f_{RF} is the maximum input RF signal frequency [2]. Since time stretch reduces f_{RF} into f_{RF}/M. it renders the ADC less sensitive to jitter-induced noise in the digitizer. Quantitatively, the jitter-limited SNR improves by 6 dB per octave of time stretch. This is an important distinguishing property of the time stretch compared with time-interleaved architectures (Fig. 1).

It should be noted that in the time-stretch system, there exist two potential types of timing jitters: optical jitter from pulsed laser and electronic jitter from digitizer's sampling clock. In the time-limited application where a single digitizer is sufficient, optical jitter does not influence the system in that only a single optical pulse is used; therefore, the RF signal is not influenced by the jitter between optical pulses. Optical jitter does change the absolute-time instant of samples. In a parallel time-stretch system where multiple segments are concatenated, optical pulse jitter is important. The influences of interpulse timing errors on the RF signal fidelity are discussed in detail in [8] and [12].

Since the shot- and thermal-noise-limited SNR is unaffected by the time-stretch process, the system, from the SNR point of view, can be treated as an RF fiber-optic link [13]. The losses in a link generally consist of electrical-to-optical (E/O) and O/E conversion losses and insertion loss of optical components. A practical time-stretch system uses optical amplifiers to compensate for the optical losses. Similar to an amplified optical link, the amplified spontaneous emission (ASE) noise is a concern.

The signal-ASE beat-noise-limited SNR can be expressed as

$$\mathrm{SNR}_{\mathrm{ASE}} = \frac{m^2/2\,(R_{\mathrm{PD}}P_s)^2}{2(R_{\mathrm{PD}}P_s)(R_{\mathrm{PD}}\rho_{\mathrm{ASE}})B_e} = \frac{m^2/2 \cdot P_s}{2\rho_{\mathrm{ASE}}B_e} \tag{8}$$

where P_s is the optical signal power, ρ_{ASE} is the ASE power spectral density, and R_{PD} is responsivity of the PD. In addition, m is the modulation index defined as $m = \pi V_{\mathrm{RF}}/V_\pi$, and V_{RF} and V_π are the RF voltage amplitude and the half-wave voltage, respectively. After time stretching, both P_s and B_e are reduced by the same factor M; hence, the signal-ASE beat-noise-limited SNR remains unchanged.

Assuming a single optical amplifier is used, (8) can be rewritten in terms of the input power of optical amplifier $P_{s,\mathrm{in}}$

$$\mathrm{SNR}_{\mathrm{ASE}} = \frac{m^2/2 \cdot P_{s,\mathrm{in}}G}{2[2n_{\mathrm{sp}}h\nu(G-1)]B_e} \approx \frac{m^2/2 \cdot P_{s,\mathrm{in}}}{4n_{\mathrm{sp}}h\nu B_e} \tag{9}$$

where h is Planck's constant, ν is the optical frequency, G is the gain of the optical amplifier, and n_{sp} is the population inversion parameter with a value close to 2 for a typical amplifier. Compared with the thermal noise in (6), $4n_{\mathrm{sp}}h\nu$ plays a similar role of $4kT$. In a typical situation, $T = 300$ K, $n_{\mathrm{sp}} = 2$, $\lambda = 1.55$ μm, $4n_{\mathrm{sp}}h\nu = -150$ dBm/Hz. This is much larger than $4kT = -168$ dBm/Hz and, hence, the signal-ASE beat noise will limit the SNR of the time-stretch preprocessor. As an example, in our current setup, the power spectral density of SC source at the input of the first erbium-doped fiber amplifier (EDFA) is around -18 dBm/nm with the repetition rate of 20 MHz. Assuming an optical bandwidth of 15 nm, the average input power is 0.24 mW. With $m = 40\%$, $n_{\mathrm{sp}} = 2$, $\lambda = 1.58$ μm, $B_e = 2$ GHz (after stretching), the calculated signal-ASE beat-noise-limited SNR is 39.7, or 6.3 SNR-bits. Here, the stretched signal is assumed to occupy the pulse repetition period and, hence, the signal power is equal to the average power. The effective bandwidth of TS-ADC will be 2 GHz times the stretch factor. Clearly, a SC source with a higher power spectral density is important to achieve a higher resolution. Every 12 dB increase in power spectral density will increase the ASE-limited resolution by 2 b.

The SNR analysis can be extended to the case where multiple optical amplifiers are present. The treatment and conclusions will be similar to those in long-haul optical links with cascaded optical amplifiers [14]. Since ρ_{ASE} accumulates after cascading, this suggests that proper location and gain of amplifiers is critical in maximizing the SNR. This noise should become the limiting factor if a large fiber propagating loss needs to be compensated. One can conclude that future development of low-loss

highly dispersive devices will be highly valuable to the TS-ADC system.

IV. Effect of Optical Dispersion on Fidelity of the Time-Stretched Electrical Signal

While dispersion performs the desired function of time stretch, it has other influences on the electrical signals; it has other, potentially adverse, effects as well. It is therefore imperative to fully understand and be able to quantify the influence of dispersion on electrical signal fidelity. In Section IV-A below, we present the mathematical framework for this purpose. Section IV-B investigates dispersion penalty and harmonic distortion caused by dispersion. Section IV-C reveals the higher order effects, which we term "residual phase errors." Finally, time stretching using SSB modulation is discussed and compared with the DSB-modulated case.

A. Mathematical Framework

In this subsection, we develop a comprehensive mathematical model for the time-stretch systems. The model is capable of predicting fundamental and higher order phenomena that modify the electrical signal during the time-stretch process.

We assume the optical SC pulse is transform-limited and has a Gaussian envelope. In frequency domain, its electric field can be represented as

$$E_1(\omega) = E_0(2\pi T_0^2)^{1/2} \exp\left(\frac{-\omega^2 T_0^2}{2}\right) \tag{10}$$

where T_o is the pulse half-width and E_o is the pulse amplitude. E_1 indicates the electrical field at the output of the SC source in Fig. 3. After propagating through the first spool of fiber, the field becomes [15]

$$E_2(\omega) = E_1(\omega) \exp\left(\frac{j\beta_2\omega^2 L_1}{2} + \frac{j\beta_3\omega^3 L_1}{6}\right) \tag{11}$$

where β_2 and β_3 are the second-order and third-order GVD, respectively. E_2 indicates the electrical field before the modulator in Fig. 3. Assuming a push–pull Mach–Zehnder modulator (MZM) biased at the quadrature point, after modulation by the sinusoid RF signal of angular frequency $\omega_{\rm RF}$, the field can be represented (in time domain) as

$$E_3(t) = E_2(t)\cos\left(\frac{\pi}{4} + \frac{m}{2}\cos\omega_{\rm RF}t\right). \tag{12}$$

E_3 is the electrical field at the output of modulator in Fig. 3. After propagation through the second fiber, the field becomes

$$E_4(\omega) = E_3(\omega)\exp\left(\frac{j}{2}\beta_2\omega^2 L_2 + \frac{j}{6}\beta_3\omega^3 L_2\right). \tag{13}$$

E_4 is the electrical field in the PD in Fig. 3. Finally, the photocurrent is given by

$$I(t) = KE_4(t)E_4^*(t) \tag{14}$$

where $K = (c\varepsilon_0 n/2)R_{\rm PD}A_{\rm eff}$, $R_{\rm PD}$ is the detector responsivity, n is the refractive index, c is the speed of light, ε_0 is the vacuum permittivity, and $A_{\rm eff}$ is the fiber-effective-mode area.

Next, we analyze the signal in the electrical domain using analytical approximations to the previously described model and verify their accuracy by comparison with numerical simulations. In Section IV-B, we consider the influence of the linear dispersion on spectrum of the electrical system. We show that linear dispersion will result in a frequency-dependent attenuation as well as frequency-dependent harmonic distortion in the time-stretched electrical signal. In Section IV-C, we consider the influence of nonlinear dispersion and describe the resulting residual phase error.

B. Dispersion Penalty and Harmonic Distortion

In this subsection, we describe and quantify dispersion-induced power penalty and harmonic distortion in the time-stretch system. Since this effect originates from the linear dispersion β_2, we temporarily neglect the nonlinear dispersion term β_3.

Using Bessel functions, (12) can be expanded as

$$E_3(t) = \frac{\sqrt{2}}{2}E_2(t)\left[J_0\left(\frac{m}{2}\right) + \sum_{n=1}^{\infty} 2c(n)J_n\left(\frac{m}{2}\right)\cos(n\omega_{\rm RF}t)\right] \tag{15}$$

where $c(n) = \begin{cases} (-1)^{n/2}, & n = \text{ even} \\ (-1)^{n+1/2}, & n = \text{ odd}. \end{cases}$

Combining (15) with (10), (11), and (13), the electrical field entering the PD can be written as (16), shown at the bottom of the page, where the envelope function $E_{\rm env}(\omega)$ corresponds to the electrical field when $m = 0$, and $\phi_{\rm DIP} = (1/2)\beta_2(L_2/M)\omega_{\rm RF}^2$ is the dispersion-induced phase (DIP). As will be shown in this paper, DIP plays a central role on the distortion in the stretched signal, whether in the DSB or

$$E_4(\omega) \approx J_0\left(\frac{m}{2}\right)E_{\rm env}(\omega) + \sum_{n=1}^{\infty} c(n)J_n\left(\frac{m}{2}\right)\exp(jn^2\phi_{\rm DIP})\left[E_{\rm env}\left(\omega - \frac{n\omega_{\rm RF}}{M}\right) + E_{\rm env}\left(\omega + \frac{n\omega_{\rm RF}}{M}\right)\right]$$
$$E_{\rm env}(\omega) = \frac{\sqrt{2}}{2}E_0(2\pi T_0^2)^{1/2}\exp\left[-\frac{\omega^2 T_0^2}{2} + \frac{j}{2}\beta_2\omega^2(L_1 + L_2)\right] \tag{16}$$

SSB modulation. In obtaining (16), the following relation was used:

$$\frac{1}{2}\beta_2 L_1(\omega-\omega_{\rm RF})^2+\frac{1}{2}\beta_2 L_2\omega^2 = \frac{1}{2}\beta_2(L_1+L_2)\left(\omega-\frac{\omega_{\rm RF}}{M}\right)^2+\phi_{\rm DIP}.$$

In the expression for $\phi_{\rm DIP}$, terms related to T_0 are neglected. This is equivalent to assuming an infinite optical bandwidth or, more precisely, $\omega_{\rm opt}\gg\omega_{\rm RF}$. This approximation is removed in the next section, and it is shown that having a finite optical bandwidth results in a subtle phenomenon, which we term the "aperture effect."

We now invoke the following property of Bessel functions: $J_n(m)\approx(1/2^n n!)m^n$. Hence, $J_p(m)J_q(m)\approx(1/2^{p+q}p!q!)m^{p+q}$. We substitute (16) into (14) and for each harmonic, we keep terms with the lowest $(p+q)$. For example, for the dc term, this requires $J_0^2(m/2)\gg 2\sum_{n=1}^{\infty}J_n^2(m/2)$. The photocurrent, so obtained, can be expressed as

$$\begin{aligned}I(t)=I_{\rm Envelope}\times\Bigg[&J_0^2\left(\frac{m}{2}\right)\\&-4J_0\left(\frac{m}{2}\right)J_1\left(\frac{m}{2}\right)\cos\phi_{\rm DIP}\cos\frac{\omega_{\rm RF}}{M}t\\&+\left[2J_1^2\left(\frac{m}{2}\right)-4J_0\left(\frac{m}{2}\right)J_2\left(\frac{m}{2}\right)\cos4\phi_{\rm DIP}\right]\\&\cdot\cos\frac{2\omega_{\rm RF}}{M}t+\left[4J_0\left(\frac{m}{2}\right)J_3\left(\frac{m}{2}\right)\cos9\phi_{\rm DIP}\right.\\&\left.+\;4J_1\left(\frac{m}{2}\right)J_2\left(\frac{m}{2}\right)\cos3\phi_{\rm DIP}\right]\cos\frac{3\omega_{\rm RF}}{M}t+\cdots\Bigg]\end{aligned}\tag{17}$$

where

$$I_{\rm Envelope}=\frac{1}{2}KE_0^2\frac{1}{\left[\frac{1+(L_1+L_2)^2}{L_D^2}\right]^{1/2}}\cdot\exp\left(-\frac{t^2}{T_0^2\left[1+\frac{(L_1+L_2)^2}{L_D^2}\right]}\right)$$

is the static ($m=0$) photocurrent, and $L_D=T_0^2/|\beta_2|$ is the dispersion length. In the case when the modulation index m is small, (17) can be simplified into

$$\begin{aligned}I(t)=I_{\rm Envelope}\times\Bigg[&1-m\cos\phi_{\rm DIP}\cos\frac{\omega_{\rm RF}}{M}t\\&+\frac{m^2}{8}(1-\cos4\phi_{\rm DIP})\cos2\frac{\omega_{\rm RF}}{M}t\\&+\frac{m^3}{96}(\cos9\phi_{\rm DIP}+3\cos3\phi_{\rm DIP})\cos3\frac{\omega_{\rm RF}}{M}t+\cdots\Bigg].\end{aligned}\tag{18}$$

The second term in (18) is the desired time-stretched signal, and the following terms describe undesired harmonics of it. The desired signal contains a frequency-dependent attenuation described by the $\cos\phi_{\rm DIP}$ term. For baseband signals, the system has a low-pass transfer function where high RF frequencies are attenuated. This is caused by interference between the beating of carrier with the upper and the lower sidebands [7]. Qualitatively, this penalty is similar to that observed in a conventional RF fiber-optic link [16]. However, its magnitude is reduced by the stretch factor M appearing in $\phi_{\rm DIP}$[7]. The reduction in the dispersion penalty occurs because as the signal travels along the length of the fiber, its modulation frequency is reduced, hence, a reduction in dispersion penalty. Based on the similarity of this effect to that in an analog optical link, SSB modulation has been proposed as a means to mitigate this effect [17].

These results were obtained for a zero-chirp modulation achievable with a push–pull MZM, as described in (12). The RF bandwidth will be higher when chirped modulation is employed. When the chirp introduced by the modulator is opposite to that introduced by fiber dispersion, the dispersion penalty can be mitigated. Chirped modulation can be achieved using a single-arm MZM biased at the quadrature point. In this case, the $\cos\phi_{\rm DIP}$ in (18) should be replaced by $\cos(\phi_{\rm DIP}\pm\pi/4)$, where the sign depends on the polarity of the bias. When the sign of the first term is opposite to the second term, the 3-dB RF bandwidth of the time-stretch system is equal to $\Delta f_{\rm RF}=[1/(4\pi|\beta_2|L_2/M)]^{1/2}$, which is 41.4% larger than the zero-chirp case $\Delta f_{\rm RF}=[1/(8\pi|\beta_2|L_2/M)]^{1/2}$ [18].

The third and forth terms in (18) are responsible for second- and third-order harmonic distortion, respectively. The amplitudes are $(m^2/8)(1-\cos4\phi_{\rm DIP})^2$ for the second harmonic and $(m^3/96)(\cos9\phi_{\rm DIP}+3\cos3\phi_{\rm DIP})$ for the third harmonic. Fig. 6(a) shows the fundamental and second harmonic power in the time-stretch system with a stretch factor $M=5$ (dashed line) as well as the same for a conventional fiber-optic link (solid line). The latter describes a case where the RF signal is modulated onto a single-wavelength carrier and travels through a fiber of length L_2. For an MZM biased at the quadrature bias point, the second harmonic is suppressed. This occurs because the second harmonics in the optical field spectrum are cancelled in the PD by those arising from the beating of the upper and lower fundamental sidebands. As the RF frequency is increased, the phase shift induced by dispersion renders this cancellation incomplete, resulting in residual second harmonic tones in the RF spectrum. The frequency dependence is periodic, as suggested by (18). Second-order distortion is not a concern in systems operating in the sub-octave bandwidth regime. In addition, while the dispersion-induced phase shift results in second-order distortion in the time-stretch system, its magnitude is far less than that in a conventional RF fiber-optic link.

Fig. 6(b) shows the same for the third harmonic distortion. At very low frequency, the third harmonic is due to the nonlinear transfer function of the modulator (biased at quadrature). Dispersion-induced phase shift results in a periodic behavior for the third-order distortion, as predicted by (18).

We note that in the limit of L_1 approaching infinity, the time-stretch system reduces to a conventional RF fiber-optic link, consisting of an externally modulated narrow-band source (e.g., distributed feedback laser) that propagates over a fiber of length L_2. In this situation, over the limited system time aperture, the source in the time-stretch system appears to be narrow band as in the conventional RF fiber-optic link. Mathematically, the stretch factor M approaches unity with $\phi_{\rm DIP}=(1/2)\beta_2 L_2\omega_{\rm RF}^2$. Equation (18) then becomes the same as the results obtained for the

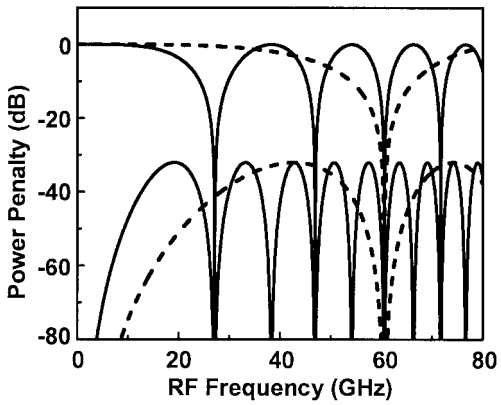

(a)

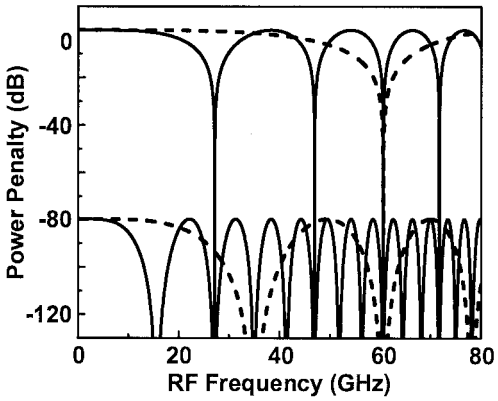

(b)

Fig. 6. (a) Electrical power transfer function for the fundamental frequency and second harmonic distortion. (b) Same for fundamental frequency and third harmonic distortion. The dashed line is for the time-stretched system, and the solid-line is for a conventional RF fiber-optic link. Calculations are for zero-chirp modulation. $L_2 = 5$ km, $M = 5$, $m = 5\%$.

dispersion penalty in a conventional RF fiber-optic link [16], [19].

C. Residual Phase Errors

In this subsection, we remove two assumptions made in the derivation of (18), i.e., ignoring third-order dispersion β_3 and also terms related to T_o in the expression for $\phi_{\rm DIP}$. At the same time, the modulation is assumed linear to simplify the mathematical analysis.

Under the assumption of linear modulation, (12) can be simplified into

$$E_3(t) \approx \frac{\sqrt{2}}{2} E_2(t) \left[J_0\left(\frac{m}{2}\right) - 2J_1\left(\frac{m}{2}\right) \cos(\omega_{\rm RF} t) \right] \quad (19)$$

where $E_2(t)$ is given by (11). Combining (19) with (10), (11), and (13), the signal entering the PD can be written as

$$\begin{aligned} E_4(\omega) = {} & J_0\left(\frac{m}{2}\right) E_{\rm env}(\omega) - J_1\left(\frac{m}{2}\right) E_{\rm env}\left(\omega - \frac{\omega_{\rm RF}}{M}\right) \\ & \cdot \exp[j\phi(-\omega_{\rm RF})] \\ & - J_1\left(\frac{m}{2}\right) E_{\rm env}\left(\omega + \frac{\omega_{\rm RF}}{M}\right) \exp[j\phi(\omega_{\rm RF})] \end{aligned} \quad (20)$$

where the envelope function is

$$\begin{aligned} E_{\rm env}(\omega) = {} & \frac{\sqrt{2}}{2} E_0 (2\pi T_0^2)^{1/2} \\ & \cdot \exp\left(-\frac{\omega^2 T_0^2}{2} + \frac{j}{2}\beta_2 \omega^2 (L_1 + L_2) + \frac{j}{6}\beta_3 \omega^3 (L_1 + L_2) \right). \end{aligned}$$

Compared with the same name function in (16), β_3 terms are included here. As shown in (20), the optical field spectrum consists of DSBs at the stretched RF frequency. This is the desired time-stretch signal. The nonideal effects, caused by dispersion, are contained in the phase of the upper and lower stretched sidebands. For the lower ($-\omega_{\rm RF}$) and upper ($+\omega_{\rm RF}$) sidebands

$$\begin{aligned} \phi(\mp\omega_{\rm RF}) = {} & \phi_{\rm DIP} + \left[3\omega\omega_{\rm RF}^2 \left(1 - \frac{1}{M}\right) \right. \\ & \left. \mp \omega_{\rm RF}^3 \left(1 - \frac{1}{M^2}\right) \right] \frac{1}{6}\beta_3 L_1 \\ & - \frac{j}{2} \left[\pm 2 \frac{\omega\omega_{\rm RF}}{\omega_{\rm opt}^2} \left(1 - \frac{1}{M}\right) - \frac{\omega_{\rm RF}^2}{\omega_{\rm opt}^2} \left(1 - \frac{1}{M^2}\right) \right] \\ \approx {} & \phi_{\rm DIP} + \frac{1}{2}\beta_3 \omega \omega_{\rm RF}^2 \frac{L_2}{M} \mp j \frac{\omega\omega_{\rm RF}}{\omega_{\rm opt}^2} \left(1 - \frac{1}{M}\right) \end{aligned} \quad (21)$$

where $\omega_{\rm opt} = 1/T_o$ is optical bandwidth (half-width at $1/{\rm e}$ intensity point).

The phase $\phi(\mp\omega_{\rm RF})$ in (21) is composed of three terms. The first term is the phase distortion due to linear dispersion β_2, which causes attenuation at high frequencies, discussed in the previous section. The second term is the phase distortion caused by β_3, which combined with the first term, creates a wavelength-dependent (and, hence, time-dependent) attenuation for a given frequency. The third term is error caused by the finite optical bandwidth.

The photocurrent in time domain can be expressed as (see Appendix)

$$\begin{aligned} I(t) = {} & I_{\rm Envelope} \\ & \times \left[\begin{array}{c} J_0^2\left(\frac{m}{2}\right) - 4J_0\left(\frac{m}{2}\right) J_1\left(\frac{m}{2}\right) \\ \left(\cos\phi_{\rm DIP} \cos\frac{\omega_{\rm RF}}{M} t + {\rm Err}_{\beta 3} + {\rm Err}_{\rm BW}\right) \end{array} \right] \end{aligned} \quad (22)$$

$${\rm Err}_{\beta_3} = -\frac{\beta_3 \omega_{\rm RF}^2 \left(1 - \frac{1}{M}\right) \sin\phi_{\rm DIP}}{2\beta_2 M} t \cos\left(\frac{\omega_{\rm RF}}{M} t\right) \quad (23)$$

$${\rm Err}_{\rm BW} = \frac{\omega_{\rm RF}\left(1 - \frac{1}{M}\right) \sin\phi_{\rm DIP}}{\omega_{\rm opt}^2 \beta_2 (L_1 + L_2)} t \sin\left(\frac{\omega_{\rm RF}}{M} t\right). \quad (24)$$

Equations (23) and (24) are the errors due to β_3 and finite optical bandwidth, respectively.

We now show the individual effects of these sources of error on a single-tone RF signal. Fig. 7(a) is a plot of $(\cos\phi_{\rm DIP} \cos(\omega_{\rm RF}/M)t + {\rm Err}_{\beta 3})$ and shows the influence of β_3 on the stretched signal, in time domain. To highlight the β_3 impact, we use a value $\beta_3 = 10$ ps^3/km that is two orders of magnitude higher than that in the SMF (SMF-28). As suggested by (23), this introduces a deleterious linear amplitude modulation. In the previous section, it is shown that β_2 introduces attenuation at high RF frequencies. The

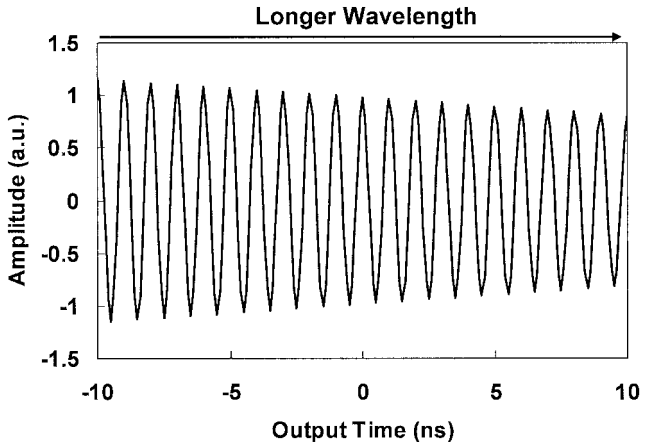

(a)

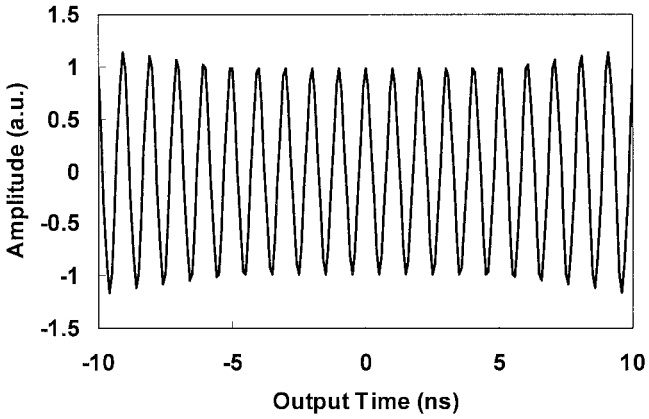

(b)

Fig. 7. (a) Influence of nonlinear GVD, characterized by β_3, on the time-stretched signal. A 100 × larger β_3 than SMF-28 is used. The behavior can be understood in terms of a wavelength-dependent dispersion penalty, causing higher attenuation at longer wavelengths. (b) Time-stretched output signal when the effect of finite optical bandwidth is included. $\omega_{\mathrm{RF}} = 10$ GHz, $M = 10$, $\beta_2 = -20\,\mathrm{ps}^2/\mathrm{km}$, $\beta_3 = 10\,\mathrm{ps}^3/$ km, $L_2 = 50$ km, $\Delta\lambda = 0.5$ nm.

influence of β_3 is to make β_2 wavelength sensitive and, hence, via wavelength-to-time mapping, cause a time-dependent attenuation. To verify the validity of approximations made and conclusion of the analytical model, numerical simulations were performed. Fig. 8 shows the error introduced by including β_3 in the simulations. The functional dependence is in full agreement with (23), verifying the validity of the approximations made in the derivation.

Fig. 7(b) is a plot of $(\cos\phi_{\mathrm{DIP}}\cos(\omega_{\mathrm{RF}}/M)t + \mathrm{Err}_{\mathrm{BW}})$ and shows the effect of the error introduced by the finite optical bandwidth. For the purpose of illustration, an unusually small optical bandwidth of 0.5 nm is used to accentuate this effect. The envelope of this function behaves as $\sqrt{1+ct^2}$. In an ideal situation where the optical bandwidth is much larger than the RF bandwidth ($\omega_{\mathrm{opt}} \gg \omega_{\mathrm{RF}}$), this error will diminish, as suggested by (24). Typically, these errors are relatively small to be observed in experiments as they are masked by other sources of noise and distortion, such as the quantization noise of a wide-band electronic digitizer, the ASE noise of optical amplifiers, and spectral nonuniformity and pulse-to-pulse variations of the SC source.

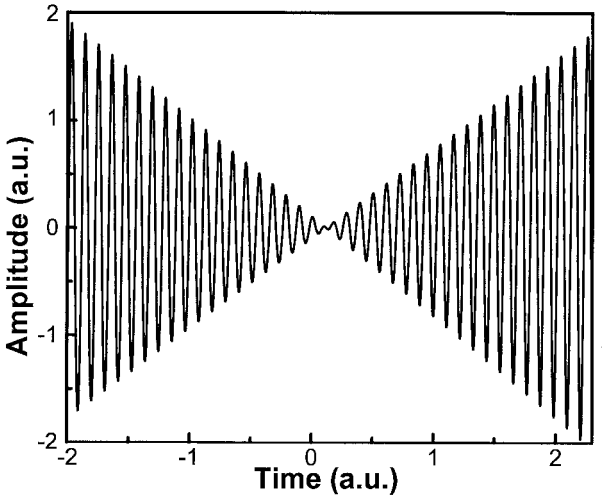

Fig. 8. Numerical simulation result showing the error caused by nonlinear GVD. The functional dependence is in full agreement with (23), verifying the validity of the approximations made in the analytical model.

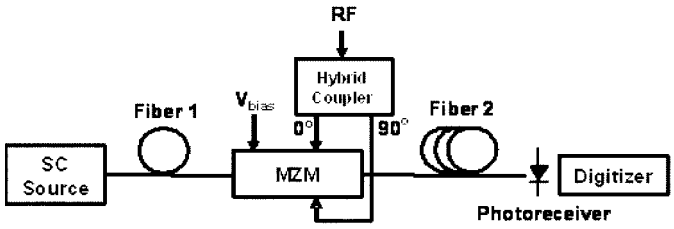

Fig. 9. Block diagram of the SSB-modulated photonic time-stretched A/D converter. The hybrid coupler provides 90° RF phase shift between its two output ports. MZM: Mach–Zehnder modulator. SC: Supercontinuum.

D. SSB Modulation

In this subsection, we provide a complete analysis of the dispersion-induced impairments in the case of SSB modulation. It extends the analysis reported in [17] by including the harmonic distortion (as in Section IV-B), the residual phase errors, including third-order dispersion and finite optical bandwidth (as in Section IV-C). SSB modulation can be achieved by using a dual-arm modulator biased at the quadrature point with the $\pi/2$ phase-shifted RF signals applied to the two arms [20]. An SSB-modulated time-stretch system is shown in Fig. 9. Under this modulation scheme, (12) is replaced by

$$E_3(t) = \frac{E_2(t)}{2}\left\{\exp\left[j\left(\frac{\pi}{2}+\frac{m}{2}\cos\omega_{\mathrm{RF}}t\right)\right]+\exp\left(j\frac{m}{2}\sin\omega_{\mathrm{RF}}t\right)\right\}. \tag{25}$$

Harmonic distortions in the SSB system can be obtained through the same procedure as in Section IV-B by replacing (15) with

$$E_3(t) = \frac{E_2(t)}{2}\sum_{n=-\infty}^{\infty}\left[(1+j^{n+1})J_n\left(\frac{m}{2}\right)\exp(jn\omega_{\mathrm{RF}}t)\right]. \tag{26}$$

If m is small, the photocurrent can be expressed as

$$I = I_{\text{Envelope}} \times \left[1 - \frac{m}{\sqrt{2}}\cos\left(\frac{\omega_{\text{RF}}}{M}t - \phi_{\text{DIP}} + \frac{\pi}{4}\right) + \frac{m^2}{8}\sin 4\phi_{\text{DIP}}\cos 2\frac{\omega_{\text{RF}}}{M}t + \frac{\sqrt{2}m^3}{192}\cos\left(3\frac{\omega_{\text{RF}}}{M}t + 9\phi_{\text{DIP}} - \frac{\pi}{4}\right) - \frac{\sqrt{2}m^3}{128}\cos\left(3\frac{\omega_{\text{RF}}}{M}t - 3\phi_{\text{DIP}} + \frac{\pi}{4}\right) + \cdots\right]. \quad (27)$$

The first two terms describe the results reported in [17]. The remaining terms are the harmonic distortion in the SSB modulation, reported here for the first time. Clearly, there is no β_2-induced attenuation in the SSB system. However, a nonlinear phase distortion is introduced through the term ϕ_{DIP}. In the context of TS-ADC, the phase distortion could be removed in the digital domain using the known dispersion behavior of the fiber. This process is facilitated by the fact that, because interference of the sidebands is avoided, signal power at the ADC input is preserved and, hence, this side effect is tolerable. Therefore, the usefulness of the SSB technique will largely depend on the effectiveness of digital correction of the phase distortion. In addition, harmonics distortion observed in the DSB modulation also appears in SSB modulation.

Similarly, the residual phase distortions in the SSB system can be obtained through the same procedure as in Section IV-C by replacing (19) with

$$E_3(t) \approx E_2(t)\left[\frac{1+j}{2}J_0\left(\frac{m}{2}\right) - J_1\left(\frac{m}{2}\right)\exp(-j\omega_{\text{RF}}t)\right]. \quad (28)$$

The photocurrent is then given by

$$I(t) = I_{\text{Envelope}} \times \left\{J_0^2\left(\frac{m}{2}\right) - 2\sqrt{2}J_0\left(\frac{m}{2}\right)J_1\left(\frac{m}{2}\right) \cdot \left[\cos\left(\frac{\omega_{\text{RF}}}{M}t - \phi_{\text{DIP}} + \frac{\pi}{4}\right) + \text{Err}_{\beta 3} + \text{Err}_{\text{BW}}\right]\right\} \quad (29)$$

$$\text{Err}_{\beta_3} = \frac{\beta_3\omega_{\text{RF}}^2\left(1 - \frac{1}{M}\right)}{2\beta_2 M}t\sin\left(\frac{\omega_{\text{RF}}}{M}t - \phi_{\text{DIP}} + \frac{\pi}{4}\right) \quad (30)$$

$$\text{Err}_{\text{BW}} = \frac{\omega_{\text{RF}}\left(1 - \frac{1}{M}\right)}{\omega_{\text{opt}}^2\beta_2(L_1 + L_2)}t\cos\left(\frac{\omega_{\text{RF}}}{M}t - \phi_{\text{DIP}} + \frac{\pi}{4}\right). \quad (31)$$

Although the attenuation of the fundamental frequency due to β_2 is eliminated, the errors due to β_3 and due to the finite optical bandwidth remain. In fact, the amplitude of these errors are larger in SSB modulation, by the factor $\sin\phi_{\text{DIP}}$ compared with DSB modulation. This is because, in the DSB modulation, the interference between two carrier-sideband beating terms partially cancels such a distortion. In the SSB modulation, the β_3 error could also be visualized as a weak dependence of the stretch factor on the electrical signal frequency. From a dispersion-penalty point of view, the SSB may be the preferred modulation method. However, the merits of DSB and SSB should be carefully examined in a particular system and for specific applications.

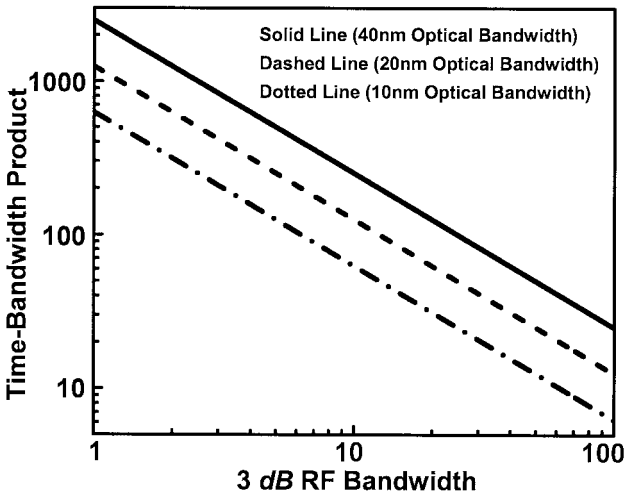

Fig. 10. Maximum achievable TBP for a given 3-dB bandwidth, in a DSB-modulated time-stretched system. Zero-chirp modulation, achieved with a push–pull MZM, is assumed.

V. Time–Bandwidth Product

A photonic time-stretch system could be described by the following three parameters: the stretch factor, time aperture, and RF bandwidth. The stretch factor is given by $M = 1 + L_2/L_1$. The time aperture is given by $T_A = \Delta\lambda D_1 L_1 = 2\pi|\beta_2|\Delta f_{\text{opt}} L_1$, where $\Delta f_{\text{opt}} = \Delta\omega_{\text{opt}}/2\pi$ is the optical bandwidth. The 3-dB RF bandwidth in the case of DSB modulation is equal to $\Delta f_{\text{RF}} = [1/(8\pi|\beta_2|L_1)]^{1/2}$ for $M \gg 1$. Naturally, it is highly desirable to maximize the time aperture. For a fixed optical bandwidth, it is possible to do so and maintain a constant stretch factor by increasing L_1 while keeping the L_2/L_1 ratio constant. However, a larger L_1 increases the dispersion penalty and reduces the RF bandwidth. This tradeoff renders neither the time aperture nor the bandwidth capable of assessing the performance alone. In this section, the product of time aperture and RF bandwidth is identified as an optimum metric to evaluate the overall performance and is analyzed for both DSB- and SSB-modulated time-stretch systems. This product also has profound significance as it reflects amounts of information contained in a segment. In addition, the limiting factor on the stretch factor is also discussed.

A. TBP for DSB Intensity Modulation

Using the previous expressions of time aperture and RF bandwidth, the TBP of the DSB-modulated system can be obtained

$$\text{TBP}_{\text{DSB}} = 2T_A\Delta f_{\text{RF}} = \frac{\Delta f_{\text{opt}}}{2\Delta f_{\text{RF}}}. \quad (32)$$

In (32), the TBP only depends on the ratio of the optical to electrical bandwidth, and this puts the fundamental limits on the achievable TBP. Fig. 10 shows the calculated TBP for a center wavelength of 1.55 μm and optical bandwidths of 10, 20, and 40 nm, respectively. Clearly, there is a tradeoff between TBP and RF bandwidth, while a broad-band DSB modulation is relatively easy to accomplish.

In a DSB-modulated time-stretch system, the TBP could be 41.4% larger than the one in (32) if chirped modulation with

proper bias, which is discussed in Section IV, is used. In addition, for passband RF signals, one may be able to operate at one of the high-frequency lobes of the transfer function. Hence, a longer L_1 could be used while maintaining a low dispersion penalty, and the time aperture of the system could be increased for a given operation frequency. However, this comes at the expense of RF bandwidth. A detailed analysis demonstrates that it does not render a larger TBP. [18]

Equation (32) indicates that a larger optical bandwidth is required to obtain a larger TBP in a DSB modulation system. In practice, the maximum SC bandwidth that can be used will depend on the wavelength response of the optical modulator. For example, in an MZM, deviation from the center wavelength results in a bias shift away from the quadrature point and a concomitant increase in second-order distortion [21]. In the multioctave system, this effect can limit the spur-free dynamic range (SFDR). As an example, for an $\mathrm{SFDR} = 80$ dB, the optical bandwidth is approximately 24 nm for an internally biased modulator. By properly choosing the physical path length mismatch and external bias, the first-order wavelength dependence of the modulator can be eliminated, removing the limitation on the optical bandwidth [21]. The wavelength dependence of the PD response is of lesser concern as it can be accurately characterized and calibrated.

B. TBP for SSB Intensity Modulation

The dispersion penalty in a DSB-modulated system arises due to dispersion-induced destructive interference between the carrier-sideband beat terms related to two sidebands. The beating occurs due to the square-law nature of the PD. As discussed in Section IV, SSB modulation could be employed for mitigating this penalty. In the context of the TBP, SSB modulation eliminates the tradeoff between the large time aperture and the large bandwidth if the nonlinear phase distortion is not concerned in the specific application. Otherwise, the same result as DSB modulation applies. The length of fiber 1 or, equivalently, the time-aperture could be freely optimized without sacrificing the RF bandwidth, assuming SSB modulation can be achieved over the entire bandwidth.

With SSB modulation, fiber dispersion will no longer limit the system bandwidth. Instead, the bandwidth of components, such as the RF hybrid coupler, will become important. In general, since the bandwidth limit is alleviated in SSB modulation, propagation loss of the fiber may become the dominant limit to TBP. The loss is proportional to the fiber length and, hence, will be proportional to the total amount of dispersion needed in the system. Using the definition of time aperture and TBP, the total fiber loss L_{TS} that is required for a given stretch factor, TBP, and RF bandwidth is given by

$$L_{\mathrm{TS}} \approx \frac{l}{D} \cdot \frac{M \cdot T_A}{\Delta\lambda} = \frac{l}{D} \cdot \frac{M \cdot \mathrm{TBP}}{2\Delta\lambda \cdot \Delta f_{\mathrm{RF}}} \tag{33}$$

for $M \gg 1$. Here, $D = (-2\pi c/\lambda^2)\beta_2$ is the dispersion parameter and l is the fiber loss per unit length. As an example, for a stretch factor $M = 10$, an RF bandwidth $\Delta f_{\mathrm{RF}} = 50$ GHz, an optical bandwidth $\Delta\lambda = 40$ nm and $\mathrm{TBP} = 1000$, the total fiber loss will be 29.4 dB if standard SMF (SMF-28) is used ($D = 17$ ps/km/ m, $l = 0.2$ dB/km). A better performance can be obtained if DCF is used ($D = -90$ ps/km/nm, $l = 0.6$ dB/km). With the DCF fiber, the loss is reduced to 16.7 dB. The tradeoff between TBP and fiber loss is shown in Fig. 11. According to (33), the loss of the dispersive elements is also the main limitation in obtaining very larger stretch factors M.

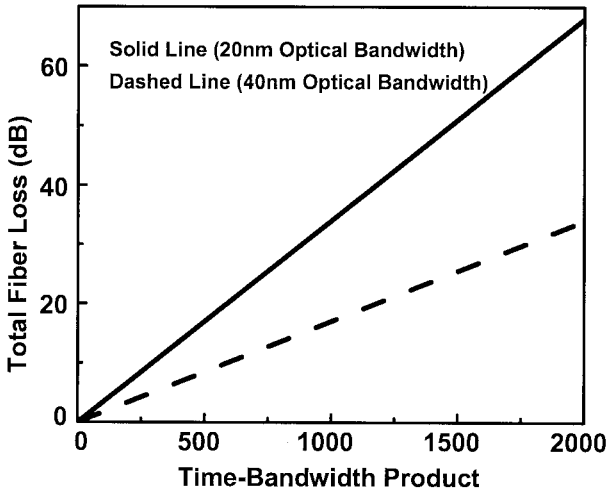

Fig. 11. Total fiber loss for a given TBP in an SSB-modulated time-stretched system. $M = 10$, $f_{\mathrm{RF}} = 50$ GHz. DCF is assumed.

We have shown that the dispersion-penalty limits the capability of a DSB-modulated TS-ADC system, by creating a tradeoff between the time aperture and RF bandwidth. A single-channel system with DSB modulation will be limited to a TBP of around 100 for a bandwidth around 10 GHz. In the application where the nonlinear phase distortion is not concerned, SSB modulation removes the tradeoff between time aperture and RF bandwidth, thus offering the potential to obtain large TBP. However, there are two practical challenges that will have to be addressed. First, as predicted by (33), the total fiber loss is proportional to the TBP and stretch factor. This will create a tradeoff between SNR and the TBP and/or stretch factor. From this point of view, dispersive devices with a superior dispersion-to-loss ratio than that obtainable with DCF will be highly desirable. Since optical amplifiers will be needed to compensate the loss, proper design of an amplified photonic time-stretched system is important. SC sources with high-power spectral densities are also desired. The second practical challenge is the ability to perform SSB modulation over a large RF bandwidth. Because the optical carrier in the time-stretched system is broad-band, traditional filtering techniques [22], [23] for SSB modulation cannot be used. Phase discrimination methods for SSB modulation require a 90° RF phase shifter. Such devices exhibit amplitude and phase ripples over a broad bandwidth [24]. This and other practical considerations are discussed in the next two sections.

VI. Practical Consideration Regarding SB Modulation

As discussed in previous sections, in the DSB-modulated TS-ADC system, the dispersion penalty results in a frequency-dependent attenuation in the electrical domain, which

arises due to destructive interference between the two carrier-sideband beat terms in the PD. Hence, SSB modulation is a potential solution. In a practical broad-band SSB modulator, only finite suppression of one of the sidebands can be accomplished. The quality of SSB modulation can be quantified by the sideband field suppression ratio, which is defined here as the ratio of amplitudes of the two sidebands. Assuming that the SSB modulator shown in Fig. 9 is used, the output optical field $E_{\rm out}(t)$ can be related to the input optical field $E_{\rm in}(t)$ by

$$\begin{aligned} &E_{\rm out}(t) \\ &= \frac{E_{\rm in}(t)}{2}\left\{\exp\left[i\left(\frac{\pi}{2}+\frac{m}{2}\cos\omega_{\rm RF}t\right)\right]\right. \\ &\quad \left.+\exp\left[i\frac{rm}{2}\sin\left(\omega_{\rm RF}t+\Delta\phi\right)\right]\right\} \\ &= \frac{E_{\rm in}(t)}{2} \\ &\quad \cdot\sum_{n=-\infty}^{\infty}\left[J_n\left(\frac{m}{2}\right)i^{n+1}+J_n\left(\frac{rm}{2}\right)\exp(in\Delta\phi)\right]\exp\left(in\omega_{\rm RF}t\right) \end{aligned} \tag{34}$$

where the modulator is biased at the quadrature point, r is the inter-electrode signal amplitude ratio (ideally equal to unity), and $\Delta\phi$ is the deviation of inter-electrode phase difference from 90°. The quality of hybrid coupler and symmetry of dual-electrode modulator are the main factors that determine r and $\Delta\phi$.

From (34), the sideband field suppression ratio R can be expressed as,

$$\begin{aligned} R &= \left|\frac{J_1\left(\frac{rm}{2}\right)\exp(i\Delta\phi)-J_1\left(\frac{m}{2}\right)}{J_1\left(\frac{rm}{2}\right)\exp(-i\Delta\phi)+J_1\left(\frac{m}{2}\right)}\right| \\ &\approx \left|\frac{r\exp(i\Delta\phi)-1}{r\exp(-i\Delta\phi)+1}\right| \end{aligned} \tag{35}$$

where the approximation is valid when the modulation index m is small. Equation (35) shows that for small modulation depths, R is independent of the modulation depth and depends only on the phase and amplitude imbalances between two arms. Over its operating bandwidth, typical imbalance parameters for a commercially available hybrid coupler are $r = \pm 0.6$ dB and $\Delta\phi = \pm 7°$(Anaren 90° hybrid coupler, Model# 10 029–3). Substituting these values into (35), we obtain $R = -10.4$ dB.

The interference between the two sideband-carrier beat signals results in the PD current of the form $I(t) \propto \cos\left(\omega_{\rm RF}t-\phi_{\rm DIP}\right)+R\cos\left(\omega_{\rm RF}t+\phi_{\rm DIP}\right)$. A detailed derivation could follow Section IV-B by replacing (15) with (34). For a DSB-modulated system where $R = 1$, it reduces to the dispersion-penalty equation, which suggests that the RF power is attentuated by $\cos^2\phi_{\rm DIP}$(as in Section IV). More generally, however, the power transfer function will depend on R based on this interference equation and will be given by

$$H = \left(\frac{1-R}{1+R}\right)^2\sin^2\phi_{\rm DIP}+\cos^2\phi_{\rm DIP}. \tag{36}$$

When $\phi_{\rm DIP} = \pi/2$, the dispersion penalty reaches its maximum value $[(1-R)/(1+R)]^2$. Fig. 12(a) shows the dispersion penalty for different sideband amplitude suppression ratios, R for a system with $L_2 = 50$ km and $M = 10$. It is evident that even with an imperfect SSB modulation, i.e., one with modest

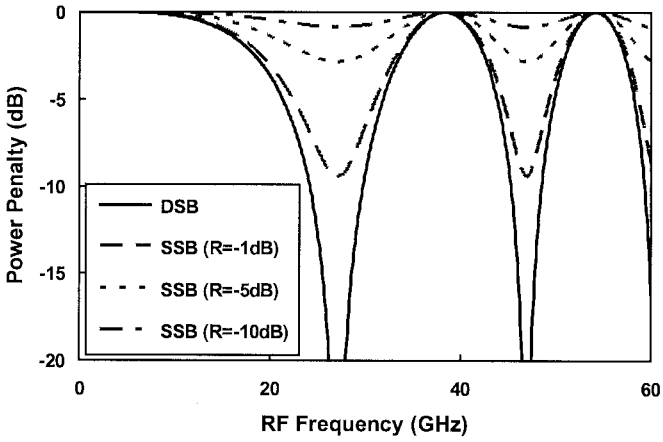

(a)

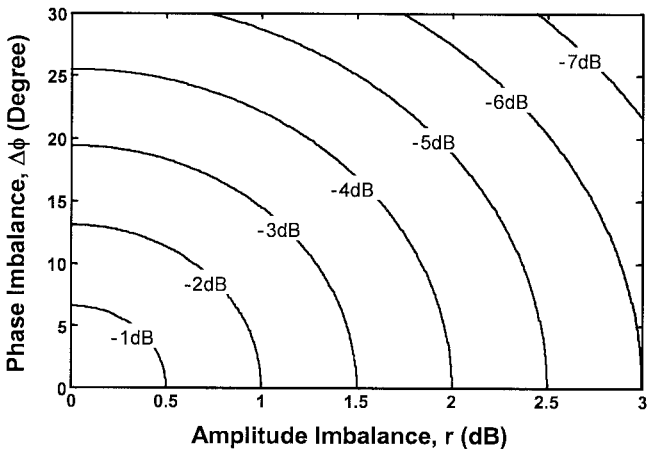

(b)

Fig. 12. (a) Dispersion-penalty curves for DSB and SSB modulation, with different sideband suppression ratios R. (b) Contour map of the maximum dispersion penalty (marker values) as a function of amplitude and phase imbalances in the SSB modulator.

SSB suppression ratio greatly reduces the dispersion penalty. As an example, when $R = -10.4$ dB, the maximum power penalty is 1.6 dB, which is acceptable for most applications.

An important consideration is the sensitivity of the dispersion penalty to physical system parameters. The contour plot in Fig. 12(b) shows the maximum power penalty as a function of amplitude and phase imbalances in the dual-arm SSB modulator. As can be observed, to obtain a power penalty of less than 3 dB, the maximum amplitude imbalance of 1.5 dB, or a maximum phase imbalance of 19° can be tolerated. This information is of critical importance in the design of the SSB-modulated TS-ADC system. Further, with $M \to 1$, the expression for the dispersion-induced-phase term $\phi_{\rm DIP}$ reduces to the same for an analog optical link of length L_2. Therefore, the analytical model developed here is equally applicable to RF fiber-optical links with the same modulation.

To investigate the performance of the SSB modulator used in the TS-ADC (Fig. 9), an external-cavity diode laser was used as the carrier so that the modulation sidebands can be examined directly in the optical spectrum analyzer. The typical modulated optical spectrum is shown in Fig. 13(a). Fig. 13(b) shows the sideband power suppression ratio ($\mathrm{SPSR} = R^2$), obtained from

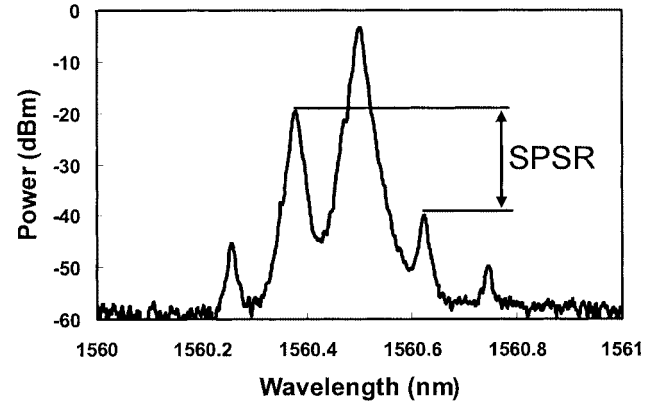

(a)

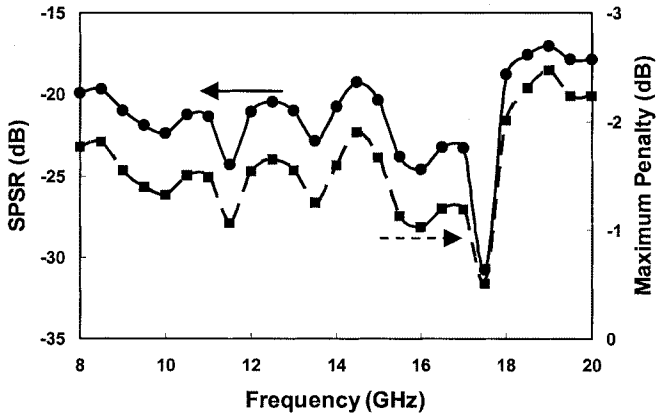

(b)

Fig. 13. (a) Measured optical spectrum of the SSB-modulated signal. The SPSR denotes the sideband power suppression ratio. (b) Measured frequency dependence of SPSR (solid line) and the corresponding maximum power penalty (dash line).

the measured optical spectrum. Results show that a minimum suppression of −18.8 dB is achieved across the bandwidth 8–18 GHz. Based on the worst-case amplitude and phase imbalances of the hybrid coupler (0.6 dB and 7° across 4–18 GHz), we calculate an $\mathrm{SPSR} = R^2 = -20.8$ dB. The difference between this and the measured value can be attributed to the imbalance in the modulator and cables, which is not considered in the theoretical value.

Also shown in Fig. 13(b) is the maximum dispersion penalty corresponding to the measured SPSR based on (36). Results indicated that the penalty can be kept below 2.5 dB, from 8–20 GHz. The lowest frequency that could be measured was limited to 8 GHz by the optical spectrum analyzer. However, since the hybrid coupler maintains the specified amplitude and phase imbalance down to 4 GHz, we conclude that the maximum penalty will be 2.5 dB across 4–20 GHz.

Fig. 14 shows a 20-GHz signal captured at 120 GSa/s with the SSB TS-ADC and the corresponding sine-wave-curve fit test. The noise bandwidth was limited to 4 GHz around 20 GHz. DCF was used as the dispersive element. The stretch factor is measured to be 5.94, the optical modulation index is 18.6%, and the input aperture is 2.9 ns. The electronic ADC is the Tektronix TDS7404 digital oscilloscope with 4-GHz input bandwidth and

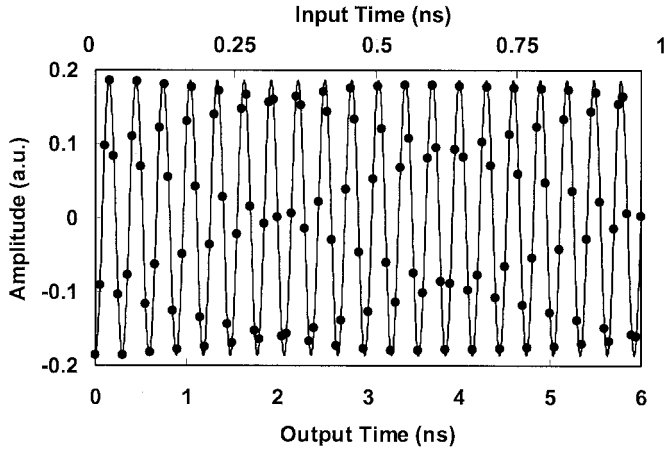

Fig. 14. 120-GSa/s real-time capture of a 20-GHz RF signal by the SSB TS-ADC system. Measured data (symbols) and fitted sine curve (solid line) of a time-stretched ADC. Effective-noise bandwidth is 4 GHz.

20 GSa/s sample rate. Therefore, the effective input sampling rate is approximately 120 GSa/s.

VII. Removal of Distortion Caused by Spectral Nonuniformities of the Optical Source

Another challenge in the TS-ADC system is the nonuniform spectral density of the SC source and its pulse-to-pulse variation. The flatness is determined primarily by that of the source as well as the influence from optical filters and the EDFA gain profile. Owing to the wavelength-to-time mapping occurring in the first fiber, spectral nonuniformities appear as a temporal modulation of the chirped pulse entering the modulator and, hence, mix with and distort the desired electrical signal. Moreover, the spectral nonuniformity is not static due to pulse-to-pulse variation of the SC source [25], [26]. To correct for these, a dynamic calibration method that is able to track the pulse-to-pulse variation is needed. In this section, a technique using a dual-output differential MZM is discussed [27]. As will be shown, this is an effective method for removing this form of distortion.

In a differential modulated system, the RF signal $s(t)$ is obtained by performing the operation

$$s(t) = \frac{1}{m}\frac{I^+(t) - I^-(t)}{I^+(t) + I^-(t)} \tag{37}$$

where $I^+(t) = (\mathrm{env}(t)/2) \cdot [1 + m \cdot s(t)]$ and $I^-(t) = (\mathrm{env}(t)/2) \cdot [1 - m \cdot s(t)]$. Here, $\mathrm{env}(t)$ is the intensity of the chirped carrier that contains unwanted temporal variations and represents the input of modulator, and $I^+(t)$ and $I^-(t)$ are the differential outputs of the MZM. One of the differential outputs follows the typical modulation equation, such as (12), with the small signal linear approximation. The other complement output could be easily obtained by the law of power conservation. Unwanted temporal variations $\mathrm{env}(t)$ arise when the nonuniform spectrum of the SC source and ripples in the optical filter are mapped into time through wavelength-to-time mapping. The subtraction and division operation remove the additive and multiplicative distortion, respectively. Since the correction is performed for each pulse, the system is immune

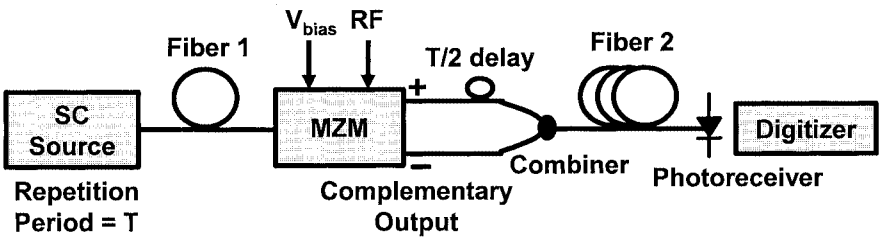

Fig. 15. Block diagram of the differential photonic time-stretched A/D converter. Repetition rate of the optical source is T. One of the outputs is delayed by $T/2$ before it is combined with the other output. Both outputs can now be captured with a single digitizer. MZM: Mach–Zehnder modulator. SC: Supercontinuum.

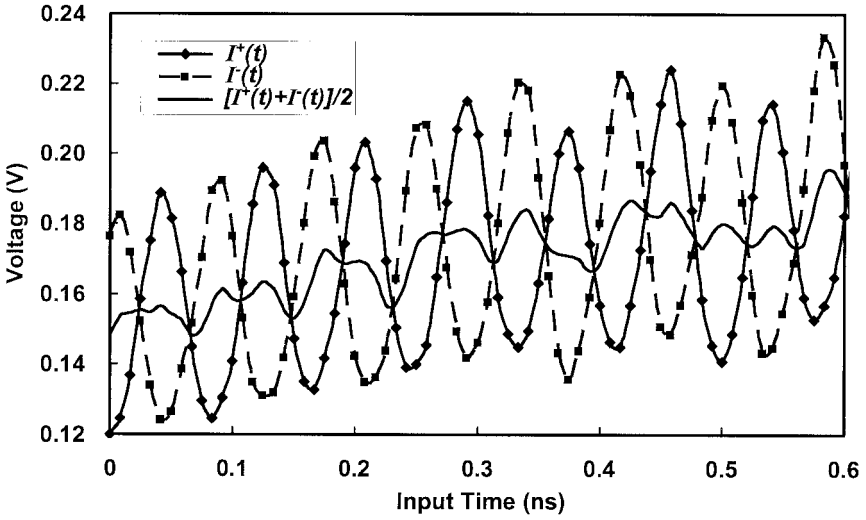

Fig. 16. Differential outputs I^+ and I^- of the modulator and their average value:$[I^+(t) + I^-(t)]/2$. The average represents the spectral shape of the optical source, including the influence of the bandpass filter.

to pulse-to-pulse variations of the SC source. We note that the differential signal processing technique described previously has been used by others for noise and distortion suppression in other types of optical systems that make use of MZMs [28].

The experimental setup is shown in Fig. 15. The SC is obtained by amplifying and passing the output of a 20-MHz passively mode-locked laser through a specialty fiber [10]. A bandpass filter selects a portion of the SC in the L band centered at 1587 nm. The L band is chosen because the source has a higher signal-to-ASE-noise ratio away from the C band. The DCF is used as the dispersive medium. An optical amplifier is inserted before the modulator to compensate for the system loss. The differential outputs of modulator are combined by a 3-dB coupler after one channel is delayed by 25 ns (half the repetition period). The electronic ADC is the Tektronix TDS7404 digital oscilloscope with 4-GHz input bandwidth and 20-GSa/s sampling rate. The stretch factor $M = 1+L_2/L_1$ of the system is 6. Therefore, the effective sampling rate of this system is 120 GSample/s.

In the experiment, a 12-GHz sinusoid signal is captured by the time-stretched ADC. Fig. 16 shows the signals from both modulator arms, i.e., $I^+(t)$ and $I^-(t)$, along with the average value $[I^+(t) + I^-(t)]/2$. The average represents the nonuniform SC envelope. Its slow variations are due to the SC source, and the fast variations originate from the ripples of the bandpass filter used to select the suitable SC portion. The gain mismatch and delay between two outputs have been calibrated. The distortion caused by the SC envelope appears as common-mode distortion of both outputs. Performing the operation described in (37) provides the waveform shown in Fig. 17, the samples, and the corresponding sine-wave-curve fit test. The sampling rate is 120 GSa/s, and the time aperture is 2.1 ns. The average SNR over 100 pulses is 22.7 ± 0.6 dB, which corresponds to 3.5 ± 0.1 b, with the 24-GHz effective-noise bandwidth. We separately characterized the digitizer with a test tone of the same amplitude as the stretched signal and equal to the digitizer's full-scale range. The measured SNR over the full bandwidth (4 GHz) was 28.8 dB, which is approximately 1 b higher than that of TS-ADC.

The differential architecture removes the distortion caused by the nonuniform SC spectrum. The remaining fundamental sources of error are the ASE-signal beat noise and the digitizer's quantization noise. In this experiment, we observe a reduction in SNR when the full-scale voltage $V_{\rm FS}$ of the quantizer is increased. This is consistent with a quantization-noise-limited performance. If A is the stretched signal amplitude, then the quantization-limited SNR is given by [29]:

$$\mathrm{SNR} = 6.02 \cdot \mathrm{ENOB} + 1.76 + 20 \log_{10} \frac{A}{V_{\rm FS}}. \qquad (38)$$

Equation (38) is also the definition of ENOB. The highest SNR is obtained when $A = V_{\rm FS}$. If $V_{\rm FS}$ is increased, the quantization-limited SNR will decrease. By contrast, the ASE-signal beat noise is independent of the ratio $A/V_{\rm FS}$. In addition, as can

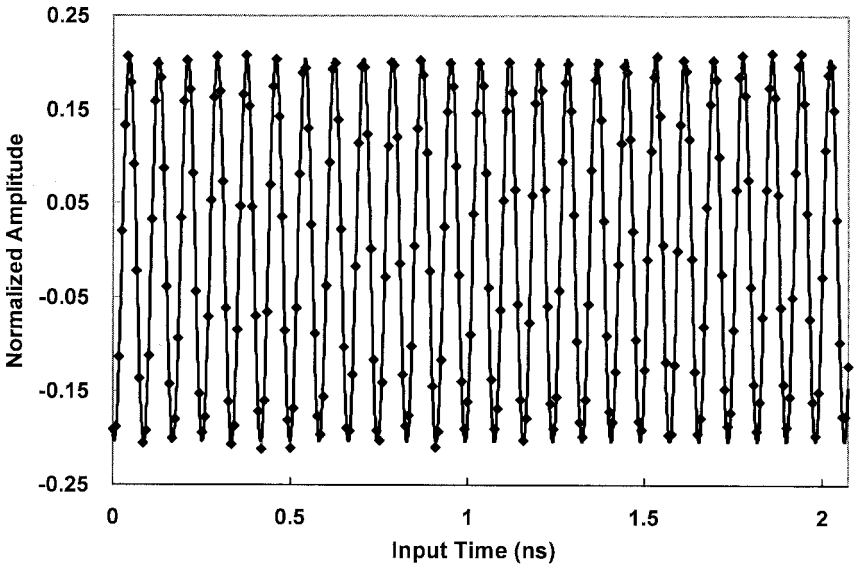

Fig. 17. 120-GSa/s real-time capture of a 12-GHz RF signal by the differential TS-ADC system. The nonuniform envelope is removed by using (37). Effective-noise bandwidth is 24 GHz.

be seen in Fig. 16, due to the nonuniform SC envelope, signals $I^+(t)$ and $I^-(t)$ could not occupy the full scale of the digitizer over the entire time aperture. Hence, $A < V_{\rm FS}$ in the experiment, resulting in a reduction in the SNR due to the increase of the quantization noise. This is the part of reason for the 1-b difference between the measured ENOB of TS-ADC and the back-to-back experiment. The fact that the SNR is not limited by the ASE represents an improvement over our previous work [9]. This has been achieved by reducing the system losses (hence, a reduction in the number of optical amplifiers) and by operating in the L-band portion of the SC where the ASE noise level is lower.

The following explanation is necessary with respect to system bandwidth in this particular experiment. In an SSB-modulated system [17], [18], the effective input bandwidth would be $4 \times 6 = 24$ GHz. In the above experiments, because of the unavailability of a dual-output SSB modulator, the experiments were performed with DSB modulation. The dispersion penalty in this system limits the input 3-dB bandwidth to 19.3 GHz. However, for quantization noise and ASE noise, the effective bandwidth is 24 GHz, independent of the modulation format (DSB or SSB).

The differential technique is one method for removing the distortion caused by spectral nonuniformities. Another method is filtering in the digital domain. If the variation caused by distortion is slow compared with the RF input signal, it can be separated from the signal in the frequency domain by low-pass filtering. The envelope so obtained can then be used to correct for the distortion. This method will place a low-frequency cutoff on the system but otherwise is able to compensate the spectral nonuniformity and its pulse-to-pulse dependence. It was employed in the SSB experiment described in Section VI.

The observation that spectral variations are mapped to similar variations in time (after dispersion) has led us to propose a new method for generating ultra wide-band electrical waveforms with arbitrary modulation [30], [31]. In this approach, the spectrum of a broad-band optical pulse is shaped according to the waveform of interest. Following dispersion, this spectral waveform is directly transformed into an identical time waveform, which is subsequently converted to electronic domain using a PD. In a recent demonstration, intelligent digital control of the spectrum has been used to render the system insensitive to the nonuniform power spectral density of the optical source [31]. The system directly converts digital data to ultra-wide-band analog waveforms.

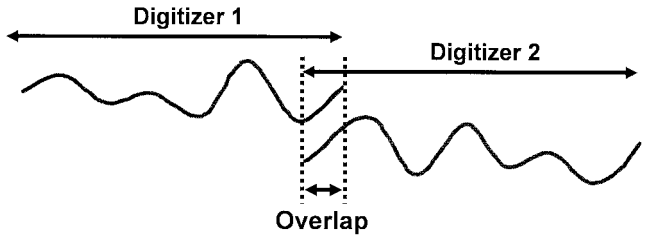

Fig. 18. Two adjacent channels of the input signal. By allowing for a finite overlap of the two channels, interchannel mismatch errors can be estimated and corrected.

VIII. Continuous-Time Operation

To fully understand the operation of the continuous-time time-stretch ADC, shown in Fig. 2(b), it is instructive to compare it with the conventional sample-interleaved ADC shown in Fig. 1. The sample-interleaved approach is the standard approach for achieving high sampling rate and is used in all such electronic digitizers. The input analog signal is simultaneously applied to a bank on M digitizers. Digitizers are then sequentially clocked at a rate of f_s/M, where f_s is the desired aggregate sampling rate. The signal is then reconstructed in the digital domain by combining sequential samples from the array of digitizers.

There are two important differences between this architecture and the continuous-time time-stretch system shown in Fig. 2(b).

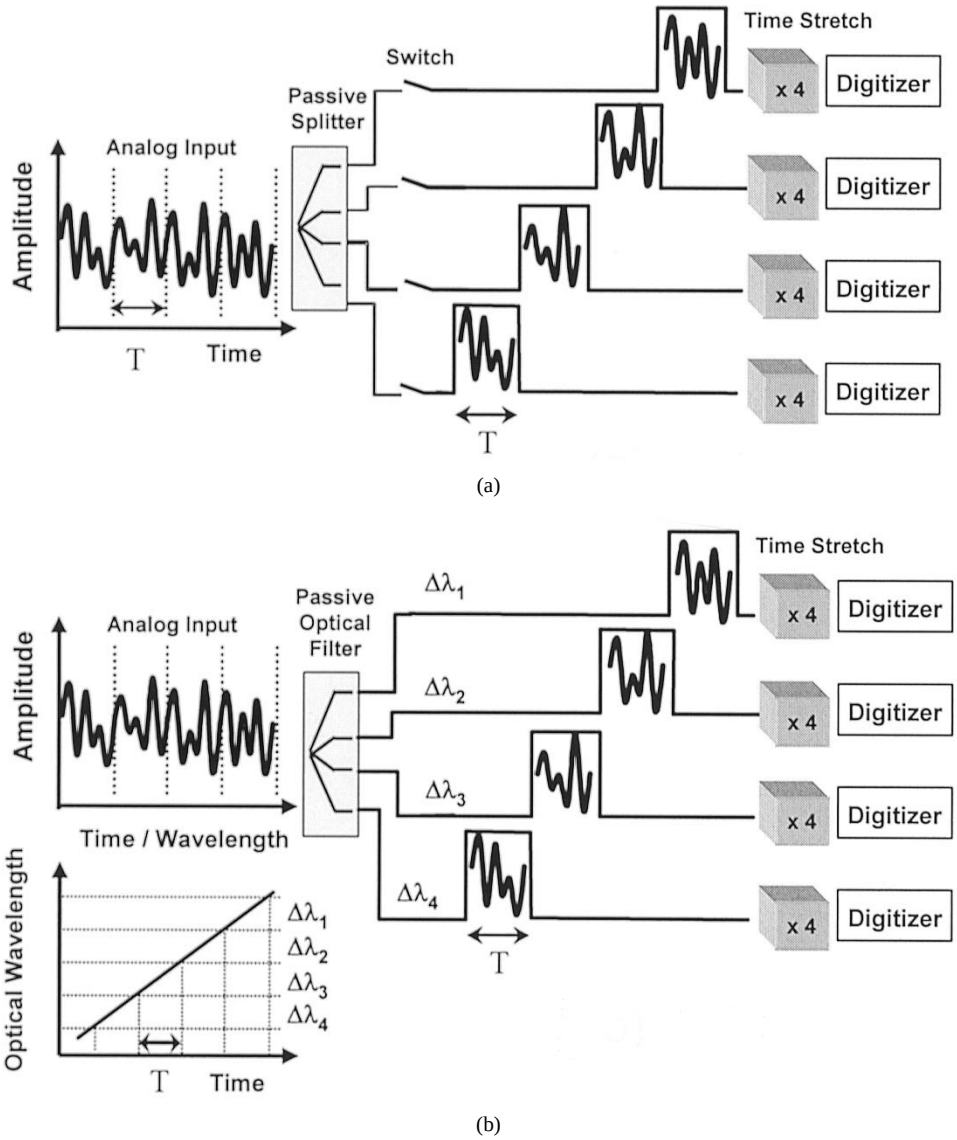

Fig. 19. Conceptual block diagrams for two possible implementations of the continuous-time time-stretch ADC. Segmentation is performed (a) using a passive splitter and time gating and (b) using a passive optical filter.

First is the fact that each digitizer in Fig. 1 sees the input signal at its full bandwidth. Although the requirement on the sampling rate for each digitizer is reduced from fs to fs/M, there is no such reduction on the required input bandwidth. Therefore, the input bandwidth of the system is not improved in this architecture. In contrast, the signal is slowed down before it enters the digitizers in the time-stretched ADC.

The second important difference between the two systems is the relative (to input frequency) sampling rate of each digitizer. In the sample-interleaved system, sampling by each digitizer is done at a fraction of the required Nyquist rate. The original signal can only be recovered *after* sample-by-sample reconstruction in the digital domain. In contrast, because the signal is slowed down prior to digitization, each digitizer samples the signal at or above the Nyquist rate in the time-stretched ADC. In other words, a time segment of the input signal is available from each digitizer *before* reconstruction. This is a significant feature of the time-stretched ADC and permits real-time cancellation of mismatch errors, as discussed subsequently.

It is well established that the performance of a sample-interleaved ADC is limited by the mismatches between different channels [3]. Interchannel gain, offset, and clock skew create spurious tones in the frequency domain and limit the dynamic range. Owing to its parallel architecture, the time-stretched ADC will also suffer from interchannel mismatch, because different segments will have to be combined to reconstruct the original signal. However, the fact that sampling in each channel meets the Nyquist criteria can be used to correct the mismatch errors. This can be achieved by allowing a finite overlap between adjacent segments, as shown in Fig. 18. By comparing signals from two adjacent digitizers in the overlap region, mismatch errors can be calculated and corrected in the digital domain [8]. Because the error is obtained from the signal itself, not from a test signal, one is able to perform real-time error correction, addressing amplitude and frequency dependencies and dynamic variations of the error. The overhead associated with the overlap will decrease with the increase in segment length and will not be significant [8].

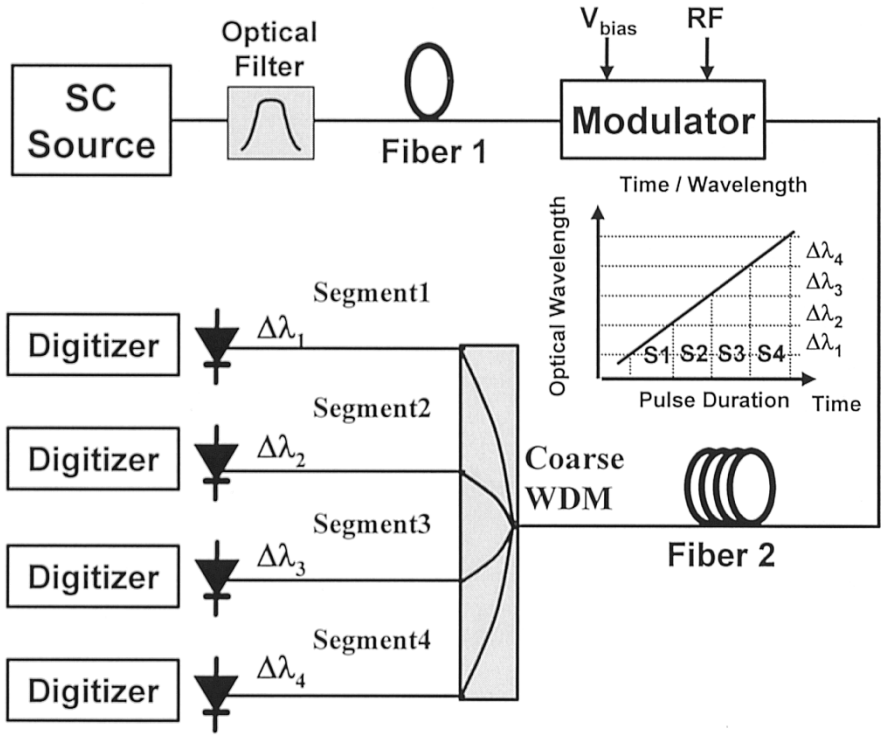

Fig. 20. Physical implementation of the continuous-time time-stretched ADC. The important feature of this design is that signals in all four channels are stretched in a single fiber, assuring identical stretch factors.

An interesting mode of operation for the continuous-time time-stretched ADC is one in which reconstruction of the signal from different segments is entirely avoided. If the segment length is sufficiently long, each segment can provide the necessary spectral information. The minimum segment length is then determined by the required resolution bandwidth. In this mode of operation, subsequent segments simply update the captured signal spectrum at the segment arrival rate. Offset mismatch manifests itself as uncertainty in the dc component between each segment. Gain mismatch affects the signal amplitude resulting in an uncertainty in the absolute value of the power spectrum. However, this does not affect the relative power of the spectral components, which is the quantity of interest in most applications. Clock (segment-to-segment timing) skew has no impact on the resulting spectrum—it will introduce a time offset. Since the segment length might not always be an integer multiple of the RF signal period, the segmentation might introduce errors similar to the leakage errors in digital signal processing. However, the error can be minimized with windowing and/or sufficiently long segments.

A central function in the continuous-time time-stretch ADC is the segmentation of the analog signal into multiple channels. Fig. 19(a) and (b) show block diagrams for two possible approaches to this function. In Fig. 19(a), the signal is split into M channels and then gated prior to the time-stretch block in each path. Segmentation is achieved by triggering the switches with a multiphase clock. In Fig. 19(b), the segmentation is performed in a completely passive method using time-to-wavelength mapping inherent in a chirped optical carrier. The RF signal is first modulated onto the chirped optical carrier, in a similar manner to that shown in Fig. 3. A passive optical filter then performs wavelength segmentation which, owing to the time-to-wavelength mapping, corresponds to the desired time segmentation. Fig. 20 shows the physical block diagram of a continuous-time time-stretched ADC, under development in our laboratory. It exploits wavelength–time mapping to perform the segmentation using passive optical filters. A key design feature of this system is the use of a single fiber (fiber 2) to stretch all four channels.

IX. Conclusion

Time-stretch preprocessing prior to digitization can mitigate many of the problems that plague ultra-wide-band A/D conversion. Currently, photonics represent the most promising approach to manipulating the time scale of an electrical signal. Since the digitization is performed in the electronic domain, this approach does not compete with electronics; it enhances it. Enhancements include an increase in the sampling rate and the input bandwidth, reduction in the digitizer sampling jitter noise, and interchannel mismatch errors.

A detailed analytical model that predicts the fidelity of the electrical output signal has been developed, and its accuracy has been verified by comparing its results with those obtained using numerical simulations. The model suggests that the fundamental performance improves with a larger optical-to-electrical-bandwidth ratio. The TBP has been identified as the proper figure of merit for comparing different architectures. With the present technology, TBP is limited to a few hundred when DSB modulation is employed. Because this limit is set by dispersion in the fiber, one can overcome it with SSB modulation if the remaining phase distortion can be corrected by an equalization

filter in the digital domain. Such a system will become loss-limited, and TBP values of several thousand can be achieved for moderated loss values (see Fig. 11). Assuming the quantization noise of the electronic digitizer is sufficiently low, the SNR of an amplified time-stretch system will be limited by the ASE-signal beat noise. To maximize the SNR, a proper design with optimum amplifier gains and locations and an SC source with high power spectral density are critical.

An important practical challenge is the nonuniform power spectral density, and pulse-to-pulse variations of the broad-band optical source used for time-to-wavelength transformation. We have presented two techniques for overcoming these challenges, both of which rely on a modest amount of signal processing in the digital domain.

To capture a continuous-time input signal, a multichannel time-stretch system is required. This architecture overcomes the TBP limitation detailed here. In principle, however, it can suffer from interchannel mismatch problems that degrade the performance of conventional sample-interleaved converters. However, there exists a fundamental difference between a parallel time-stretched array and a sample-interleaved converter array. In the latter, the signal in each channel is sampled at a fraction of the required Nyquist rate, whereas in the former, it is sampled at, or above, the Nyquist rate. This permits an effective online calibration of the mismatch errors.

APPENDIX

Here, we describe the derivation for (22)–(24).

Using (21), when the distortion is relatively small, the exponential terms $e^{j\phi(\mp\omega_{\rm RF})}$ in (20) can be written in a linear form as

$$e^{j\phi(\mp\omega_{\rm RF})} \approx \exp(j\phi_{\rm DIP})\left[1+\frac{j}{2}\beta_3\omega\omega_{\rm RF}^2\frac{L_2}{M}\pm\frac{\omega\omega_{\rm RF}}{\omega_{\rm opt}^2}\left(1-\frac{1}{M}\right)\right]. \quad \text{(A1)}$$

Use (A1) and transform (20) into the time domain. The lower sideband signal can be obtained as

$$\begin{aligned} E_{4,\rm lower}(t) &= -J_1\left(\frac{m}{2}\right)\exp(j\phi_{\rm DIP})\left[E_{\rm env}(t)\exp\left(-j\frac{\omega_{\rm RF}}{M}t\right)\right. \\ &\quad -\frac{1}{2}\beta_3\omega_{\rm RF}^2\frac{L_2}{M}\frac{d}{dt}\left[E_{\rm env}(t)\exp\left(-j\frac{\omega_{\rm RF}}{M}t\right)\right] \\ &\quad \left.+j\frac{\omega_{\rm RF}}{\omega_{\rm opt}^2}\left(1-\frac{1}{M}\right)\frac{d}{dt}\left[E_{\rm env}(t)\exp\left(-j\frac{\omega_{\rm RF}}{M}t\right)\right]\right]. \quad \text{(A2)} \end{aligned}$$

In (A2), the second and third terms correspond to the β_3 distortion and the limited optical bandwidth, respectively. To further simplify the derivative term in (A2), the third-order dispersion term in the envelope is ignored and we obtain

$$\begin{aligned} \frac{\frac{dE_{\rm env}}{dt}}{E_{\rm env}} &\approx \frac{\frac{d}{dt}\exp\left\{-\frac{t^2}{2}[I_o^2-j\beta_2(L_1+L_2)]\right\}}{\exp\left\{-\frac{t^2}{2}[I_o^2-j\beta_2(L_1+L_2)]\right\}} \\ &= \frac{-t}{I_o^2-j\beta_2(L_1+L_2)} \approx \frac{t}{j\beta_2(L_1+L_2)}. \quad \text{(A3)} \end{aligned}$$

Using (A3), it can be proven that

$$\frac{d}{dt}\left[E_{\rm car}(t)\exp\left(-j\frac{\omega_{\rm RF}}{M}t\right)\right] \approx \frac{dE_{\rm car}(t)}{dt}\exp\left(-j\frac{\omega_{\rm RF}}{M}t\right)$$

holds. The upper sideband can be similarly handled. Substituting all the results into (14), the photocurrent can be obtained

$$\begin{aligned} I(t) = I_{\rm Envelope}\times\left[J_0^2\left(\frac{m}{2}\right)-4J_0\left(\frac{m}{2}\right)J_1\left(\frac{m}{2}\right)\right. \\ \left.\cdot\left(\cos\phi_{\rm DIP}\cos\frac{\omega_{\rm RF}}{M}t+{\rm Err}_{\beta 3}+{\rm Err}_{\rm BW}\right)\right] \end{aligned} \quad \text{(A4)}$$

$${\rm Err}_{\beta_3} = -\frac{\beta_3\omega_{\rm RF}^2\left(1-\frac{1}{M}\right)\sin\phi_{\rm DIP}}{2\beta_2 M}t\cos\left(\frac{\omega_{\rm RF}}{M}t\right) \quad \text{(A5)}$$

$${\rm Err}_{\rm BW} = \frac{\omega_{\rm RF}\left(1-\frac{1}{M}\right)\sin\phi_{\rm DIP}}{\omega_{\rm opt}^2\beta_2(L_1+L_2)}t\sin\left(\frac{\omega_{\rm RF}}{M}t\right). \quad \text{(A6)}$$

ACKNOWLEDGMENT

The authors would like to thank Dr. J. Murphy and Dr. R. Leheny for their support as well as Prof. H. Fetterman, Dr. A. S. Bhushan, Dr. O. Boyraz, A. Nuruzzaman, and J. Han for helpful discussions.

REFERENCES

[1] J. A. Wepman, "Analog-to-digital converters and their applications in radio receivers," *IEEE Commun. Mag.*, vol. 33, pp. 39–45, May 1995.
[2] R. H. Walden, "Analog-to-digital converter survey and analysis," *IEEE J. Select. Areas Commun.*, vol. 17, pp. 539–550, Apr. 1999.
[3] W. C. Black and D. A. Hodges, "Time interleaved converter arrays," *IEEE J. Solid-State Circuits*, vol. SC-15, pp. 1022–1029, Dec. 1980.
[4] A. Montijo and K. Rush, "Accuracy in interleaved ADC systems," *Hewlett-Packard J.*, vol. 44, no. 5, pp. 38–46, Oct. 1993.
[5] W. J. Caputi, "Stretch: A time-transformation technique," *IEEE Trans. Aerosp. Electron. Syst.*, vol. AES-7, pp. 269–278, Mar. 1971.
[6] B. Jalali and F. Coppinger, "Data conversion using time manipulation," U.S. Patent 6 288 659, Sept. 11, 2001.
[7] F. Coppinger, A. S. Bhushan, and B. Jalali, "Photonic time stretch and its application to analog-to-digital conversion," *IEEE Trans. Microwave Theory Tech.*, vol. 47, pp. 1309–1314, July 1999.
[8] Y. Han, B. Rezaei, V. P. Roychowdhury, and B. Jalali, "Adaptive online calibration in time stretched ADC arrays," in *Proc. Instrumentation Measurement Technology Conf.*, vol. 2, 2003, pp. 1212–1216.
[9] A. S. Bhushan, P. V. Kelkar, B. Jalali, O. Boyraz, and M. Islam, "130 GSa/s photonic analog-to-digital converter with time stretch preprocessor," *IEEE Photon. Technol. Lett.*, vol. 14, pp. 684–686, May 2002.
[10] O. Boyraz, J. Kim, M. N. Islam, F. Coppinger, and B. Jalali, "Broadband, high-brightness 10-Gbit/s supercontinuum source for A/D conversion," in *Proc. Lasers Electro-Optics Conf.*, 2000, pp. 489–490.
[11] B. H. Kolner and M. Nazarathy, "Temporal imaging with a time lens," *Opt. Lett.*, vol. 14, no. 12, pp. 630–632, June 1989.
[12] B. Asuri, Y. Han, and B. Jalali, "Time-stretched ADC arrays," *IEEE Trans. Circuits Syst. II*, vol. 49, pp. 521–524, July 2002.
[13] E. I. Ackerman and C. H. Cox, "RF fiber-optic link performance," *IEEE Microwave*, vol. 2, pp. 50–58, Dec. 2001.
[14] R. Ramaswami and K. N. Sivarajan, *Optical Networks*, 2nd ed. San Mateo, CA: Morgan Kaufmann, 2002.
[15] G. P. Agrawal, *Nonlinear Fiber Optics*, 3rd ed. San Diego, CA: Academic, 2001, ch. 3.
[16] H. Schmuck, "Comparison of optical millimeter-wave system concepts with regard to chromatic dispersion," *Electron. Lett.*, vol. 31, no. 21, pp. 1848–1849, Oct. 1995.
[17] J. M. Fuster, D. Novak, A. Nirmalathas, and J. Marti, "Single-sideband modulation in photonic time-stretch analogue-to-digital conversion," *Electron. Lett.*, vol. 37, no. 1, pp. 67–68, Jan. 2001.

[18] Y. Han and B. Jalali, "Time-bandwidth product of the photonic time-stretched analog-to-digital converter," *IEEE Trans. Microwave Theory Tech.*, vol. 51, pp. 1886–1892, July 2003.
[19] A. Hilt, "Microwave harmonic generation in fiber-optical links," in *Proc. 13th Int. Conf. Microwaves, Radar Wireless Communications*, vol. 2, 2000, pp. 693–698.
[20] G. H. Smith, D. Novak, and Z. Ahmed, "Technique for optical SSB generation to overcome dispersion penalties in fiber-radio systems," *Electron. Lett.*, vol. 33, no. 1, pp. 74–75, Jan. 1997.
[21] S. Dubovitsky, W. H. Steier, S. Yegnanarayanan, and B. Jalali, "Analysis and improvement of Mach–Zehnder modulator linearity performance for chirped and tunable optical carriers," *J. Lightwave Technol.*, vol. 20, pp. 886–891, May 2002.
[22] K. Yonenaga and N. Takachio, "A fiber chromatic dispersion compensation technique with an optical SSB transmission in optical homodyne detection systems," *IEEE Photon. Technol. Lett.*, vol. 5, pp. 949–951, Aug. 1993.
[23] J. Park, W. V. Sorin, and K. Y. Lau, "Elimination of the fiber chromatic dispersion penalty on 1550 nm millimeter-wave optical transmission," *Electron. Lett.*, vol. 33, no. 6, pp. 512–513, Mar. 1997.
[24] K. Chang, I. Bahl, and V. Nair, *RF and Microwave Circuit and Component Design for Wireless Systems*. New York: Wiley, 2002.
[25] M. Nakazawa, K. Tamura, H. Kubota, and E. Yoshida, "Coherence degradation in the process of supercontinuum generation in an optical fiber," *Optical Fiber Technology*, vol. 4, no. 2, pp. 215–223, 1998.
[26] O. Boyraz, J. Kim, M. N. Islam, F. Coppinger, and B. Jalali, "10 Gb/s multiple wavelength, coherent short pulse source based on spectral carving of supercontinuum generated in fibers," *J. Lightwave Technol.*, vol. 18, pp. 2167–2175, Dec. 2000.
[27] Y. Han and B. Jalali, "Differential photonic time stretch analog-to-digital converter," presented at the Lasers and Electro-Optics Conf., Baltimore, MD, June 1–6, 2003, Paper CWH2.
[28] J. C. Twichell and R. Helkey, "Phase-encoded optical sampling for analog-to-digital converters," *IEEE Photon. Technol. Lett.*, vol. 12, pp. 1237–1239, Sept. 2000.
[29] J. G. Proakis and D. G. Manolakis, *Digital Signal Processing: Principles, Algorithms, and Applications*, 3rd ed. Englewood Cliffs, NJ: Prentice-Hall, 1996.
[30] B. Jalali, P. Kelkar, and V. Saxena, "Photonic arbitrary waveform generator," in *Proc. 14th Annu. Meeting IEEE Lasers Electro-Optics Society*, vol. 1, 2001, pp. 253–254.
[31] J. Chou, Y. Han, and B. Jalali, "Adaptive RF-photonic arbitrary waveform generator," in *Proc. Microwave Photonics Conf.*, 2002, Paper T2–1, pp. 93–96.

Yan Han received the B.S. and M.S. degrees in electronic engineering from the Tsinghua University, Beijing, China, in 1998 and 2000, respectively. He is currently working toward the Ph.D. degree with the Department of Electrical Engineering at the University of California, Los Angeles (UCLA).

His research interests include the areas of microwave photonics, optical communications, optical amplifiers, and fiber optics.

Bahram Jalali (S'86–M'89–SM'97–F'03) was a Member of Technical Staff at the Physics Research Division of AT&T Bell Laboratories, Murray Hill, NJ, from 1988 to 1992, where he conducted research on ultrafast electronics and optoelectronics. In 1992, he was responsible for successful development and delivery of 10-Gb/s lightwave circuits to the U.S. Air Force. He is currently a Professor of Electrical Engineering, the Director of the DARPA Center for Optical A/D System Technology (COAST), and the Director of the Optoelectronic Circuits and System Laboratory at the Universeity of California, Los Angeles (UCLA). While on leave from UCLA between 1999 and 2001, he founded Cognet Microsystems, a Los Angeles, CA-based fiber-optic component company that was acquired by Intel Corporation in 2001. He has more than 120 publications and holds five U.S. patents. He currently serves as a Consultant for the Wireless Networking Group (WNG) of Intel Corporation. His current research interests are in microwave photonics, integrated optics, and fiber-optic integrated circuits.

Dr. Jalali is a Member of the California Nano Sciences Institute (CNSI) and is the Chair of the Los Angeles Chapter of the IEEE Lasers & Electro-Optics Society (LEOS). He was the General Chair for the IEEE international conference on Microwave Photonics (MWP) in 2001 and its Steering Committee chair from 2001–present, and he serves on the Board of Trustees of the California Science Center. He received the BridgeGate 20 Award in 2001 in recognition of his contributions to the Southern California hi-tech economy.